Petroleum Science 23 (2026) 2773–2792

Contents lists available at ScienceDirect

Petroleum Science

journal homepage: www.keaipublishing.com/en/journals/petroleum-science

Original Paper

Hydraulic-mechanical analysis of induced stress change in unconventional reservoirs using a novel fundamental solution of poromechanics in a half space

Shihao Wang *, Ouassim Khebzegga

Chevron Corp., 1500 Louisiana Street, Houston, TX 77002, USA

ARTICLE INFO

Article history:
Received 9 October 2024
Received in revised form
19 December 2025
Accepted 28 January 2026
Available online 6 February 2026

Edited by Yan-Hua Sun

Keywords:
Fundamental solution
Geomechanics
Poroelasticity
Unconventional reservoirs
Half space

ABSTRACT

The production of fractured unconventional reservoirs induces stress changes, which will affect the production performance of neighboring wells. To quantify such effects, the analytical solution is a convenient yet accurate tool. In this work, we have developed an analytical solution of the transient pressure and stress variation induced by the production of a point/line/plane source in a semi-infinite poroelastic reservoir with a traction-free surface boundary. We have benchmarked the derived solution with both analytical solution and numerical program. The solution demonstrates excellent accuracy. Moreover, the analytical approach reduces the computational time of numerical approaches from hours to seconds. We then apply the solution to study the surface subsidence control and stress interference between fractured horizontal wells. Results show that the derived solution is capable of quantifying complex hydraulic-mechanical processes during the recovery of shallow water as well as deep shale reservoirs. Upon investigation, we have found that infill wells can effectively reduce the surface subsidence induced by the production of shallow horizontal wells. Furthermore, shale reservoirs with lower permeability are more sensitive to pressure-stress changes. The range of stress reorientation can also be efficiently quantified by the developed approach. Also, normal stresses and shear stresses behave differently during fracture driven interactions. The above findings potentially benefit the decision-making in the asset development. The major novelty of our work lies in the extension of existing approaches that are limited to axisymmetric problems to line and plane sources problems, so that the solution can be used in unconventional reservoirs with fractures.

1. Introduction

The development of oil fields or underground water reservoirs alters the in situ pressure environment, which causes the change of downhole stress. Since the stress change may drastically affect the production performance, the quantification of the induced pressure-stress fields is thus important to the reservoir management (Jaeger et al., 2007). To prompt the accurate modeling of such multiphysical processes, both numerical approaches, such as the finite element method (FEM), the discrete element method (DEM), and the boundary element method (BEM), as well as analytical approaches have been developed. FEM is particularly effective for modeling complex geological formations and heterogeneous material properties, as it discretizes the entire domain into elements and solves for the stress and displacement fields. It is commonly used to simulate wellbore stability (Ravaji et al., 2018; Akbarpour and Abdideh, 2020), reservoir compaction (Liu and Liu, 2018), and fracture propagation (Yu et al., 2019, 2023). Recently, FEM has also been adopted to study the fracture interference during the recovery of unconventional reservoirs (Wang et al., 2022c). The limitation of FEM mainly lies in its computational efficiency as it needs relatively high resolution to achieve satisfactory accuracy. DEM is valuable for analyzing stress evolution during reservoir development, where rock failure, fault activation, and fracture propagation play critical roles. DEM enables detailed representation of fracture initiation and coalescence under fluid injection or production-induced stress changes (Weng et al., 2024). It is

* Corresponding author.
E-mail addresses: shihao.wang@chevron.com, gohych@gmail.com (S. Wang).
Peer review under the responsibility of China University of Petroleum (Beijing).

https://doi.org/10.1016/j.petsci.2026.01.049

especially useful in unconventional reservoirs, such as tight sandstone or shale formations, where natural fractures and bedding planes significantly influence reservoir response. By capturing discontinuous deformation and failure mechanisms, DEM provides insights into wellbore stability, sand production, and reservoir compaction that are difficult to obtain with continuum-based approaches. Recently, DEM has also been combined with the phase field method to conduct first-principal simulation of chemical-mechanical processes (Sac-Morane et al., 2024), which makes it possible to model formation damage in the future. DEM suffers from poor scalability and becomes less reliable when applied to large scale (reservoir or field) problems. BEM, on the other hand, is advantageous for problems with infinite or semi-infinite domains, such as stress changes induced by fault activation or hydraulic fracturing, as it requires discretization only of the boundaries. Due to its reduced computational cost and ability to accurately model stress perturbations in elastic media, BEM is often employed in dynamic fracture modeling (Wu and Olson, 2016; Chen et al., 2021; Wang et al., 2023b) and complex fracture networks (Du et al., 2024). It should be noted that BEM relies on the 'fundamental solution' of the governing equation, which will be introduced next. The discrete lattice model is another appealing approach. Liu et al. (2023) developed and verified a 3D discrete lattice model to study hydraulic fracturing in a sectorial well-factory where wells deviate from the minimum horizontal stress, proposing four morphology-based indexes to quantify fracture deflection and well interference. Zhang et al. (2024) used a 3D discrete lattice method to model multiscale hydraulic fracture growth from perforations in naturally layered media. Alvarez et al. (2025)'s work modeled multi-well fracturing in the Kongdian shale using a discrete-based lattice method and microseismic data, then systematically evaluates how well geometry, lithology, natural fractures, faults, and sequencing control inter-well interference and fault reactivation. Moreover, Hui et al. (2024) investigated a Duvernay case using an unconventional fracture model with Mohr–Coulomb and coupled stress/pressure analysis.

The analytical solution is another effective tool (Selvadurai, 2007) in geomechanical modeling. Compared to numerical approaches, analytical solutions are with higher precision and less computationally-expensive. As such, analytical methods are especially appealing in the application of unconventional reservoirs in which the development pace is fast and the uncertainty is huge. In particular, the fundamental solution, a special type of the analytical solutions, captures the transient behavior of the pressure-change induced by a point source or a line source. The application of the fundamental solution lies in several aspects. Firstly, it can be adopted to rapidly delineate the depletion condition for the analysis of parent-child well interference (Manchanda et al., 2018). Secondly, it can be used for benchmarking numerical methods (Abousleiman et al., 1996). Thirdly, it is the foundation of certain numerical methods, for instance the boundary element method as mentioned above (Crouch, 1976; Dong and de Pater, 2001). Therefore, a reliable fundamental solution for the above-mentioned multiphysical process is demanding in the subsurface community.

The reservoir can be viewed as a half space with the ground surface as a traction-free boundary, and the status of the fluid flow in the reservoir rock is time-varying. In the literature, previous efforts on the fundamental solution were mostly focused on static poroelastic problems (Pan, 1989; Pan et al., 2016) or dynamic poroelastic problems in the infinite space (Cheng et al., 1991; Taguchi and Kurashige, 2002). Till now, developments on three-dimensional transient poroelastic solutions in half-space are limited. For instance, Senjuntichai and Rajapakse (1994) derived a two-dimensional dynamic Green's function for poroelastic materials in a half-plane under the plane strain condition. Segall (1992) obtained a semi-analytical solution within half-space in the cylindrical coordinate system. The solution is based on Geertsma's nuclear of strain theory (Geertsma, 1973) and is only applicable to cases where the pressure change is given. Moreover, existing approaches of point-source solutions are mostly based on the displacement potential method (Selvadurai, 2007), which inevitably involves special functions in the final formulation and is therefore difficult to be extended to line-source solutions. Senjuntichai and Rajapakse (1994) developed a fundamental solution for a three-dimensional poroelastic half-space. This solution is limited to axially symmetric cases, such as cases with point sources and ring sources. Rajapakse's solution has been extended to layered cases (Lu and Hanyga, 2005) and dynamic problems (Philippacopoulos, 1997) with axially symmetric sources. The axially symmetric sources limit the application of such solution to practical cases with horizontal wells (horizontal line sources) and fractures (plane source). In this work, we use Rajapakse's solution to validate our solution for point source cases. Given the aforementioned history, it can be seen that a general analytical solution that can handle sources with arbitrary shape in a half-space is still lacking.

In the authors' previous work (Wang et al., 2023a), we have developed an analytical solution of the pressure and stress in a rectangular domain by assuming the pressure and stress on the boundaries of the domain are constant. Although such assumptions are acceptable for deep reservoirs, they become invalid when the reservoir is relatively shallow (such as Chevron's shallow-water fields on the Pacific coast and groundwater reservoirs). In this work, we relaxed this assumption and developed a solution with multiple types of sources in a semi-infinite reservoir with a traction-free surface, which is more realistic compared to the existing works. This improvement is non-trivial as the solution method must fundamentally shift from eigenfunction expansion to integral transform techniques. Our solution approach differs with the previous works in that it can be obtained in the Cartesian coordinate system, which makes the extension to line source and plane source solutions much more convenient (Wang, 2015; Wang et al., 2017).

The novelty of our work lies in several aspects. First of all, we have developed a new approach to obtain the formulation of point-source and line source solutions in Cartesian coordinate systems in the frequency domain. In particular, the line-source solution is arguably the first of its kind. Secondly, based on the newly developed approach, we have analyzed and have discussed the mathematical structure of the solution in depth, which may shed light on the understanding of the underlying physical process.

This paper is organized as follows. In Section 2, we present the mathematical model, including the assumptions and the governing equations. The derivation of the fundamental solution, including the point source, line source and plane source solutions is also provided in this section. In Sections 3 and 4, we validate the derived solution and apply it to several case studies, respectively. At last, we show our analysis on the mathematical structure of the solution and summarize this work in Sections 5 and 6.

2. Mathematical model

In this section, we present the mathematical model of the problem of interest. We start with the presentation of the model setup and assumptions used in this work, then describe the hydraulic and mechanical governing equations.

2.1. Conceptual model

In practice, the wellbore of a vertical well and a horizontal well can be approximately treated as a point source and line source, respectively. The fracture can be viewed as a plane source. The reservoir can be mathematically described as a half-space domain. Liquid is produced from the source with a time-varying rate. The schematic models of such a system are shown in Fig. 1. For convenience, we have inverted the z axis of the coordinate system in this work, so that the 'depth' value is a positive number, which is a common practice of the subsurface engineering community. Moreover, we make the following assumptions on the rock and fluid properties in this work.

- The reservoir is semi-infinite, consisting of homogeneous, isotropic, and poroelastic rocks.
- The fluid flow in the reservoir is single phase and single component.
- The top of the reservoir is a no-flow and traction-free boundary.
- The reservoir rock permeability is constant and is not impacted by stress changes.
- The impact of the body force is ignored in this work. (We have shown in a previous work that the body force can be safely ignored for engineering problems (Wang et al., 2022b).)
- The mechanical process is static equilibrium.

We make the above assumptions due to following considerations. First of all, the poroelastic model has been widely applied in the multiphysical modeling of unconventional reservoirs (Guo et al., 2019; Wang et al. 2021, 2022c). For shale rocks, it has been reported in the literature that poroelasticity can be a sound approximation for a wide range of fields except cases where the in situ stress is extremely high (Ma and Zoback, 2017; Ma and Gutierrez, 2021). Shallow water reservoirs, on the other hand, mostly consist of sedimentary rocks, such as sandstone and dolomite (Hanak et al., 2019). The former is a typical poroelastic medium, while the latter may exhibit stronger nonlinear behavior. As such, the poroelastic assumption can be safely applied to shale

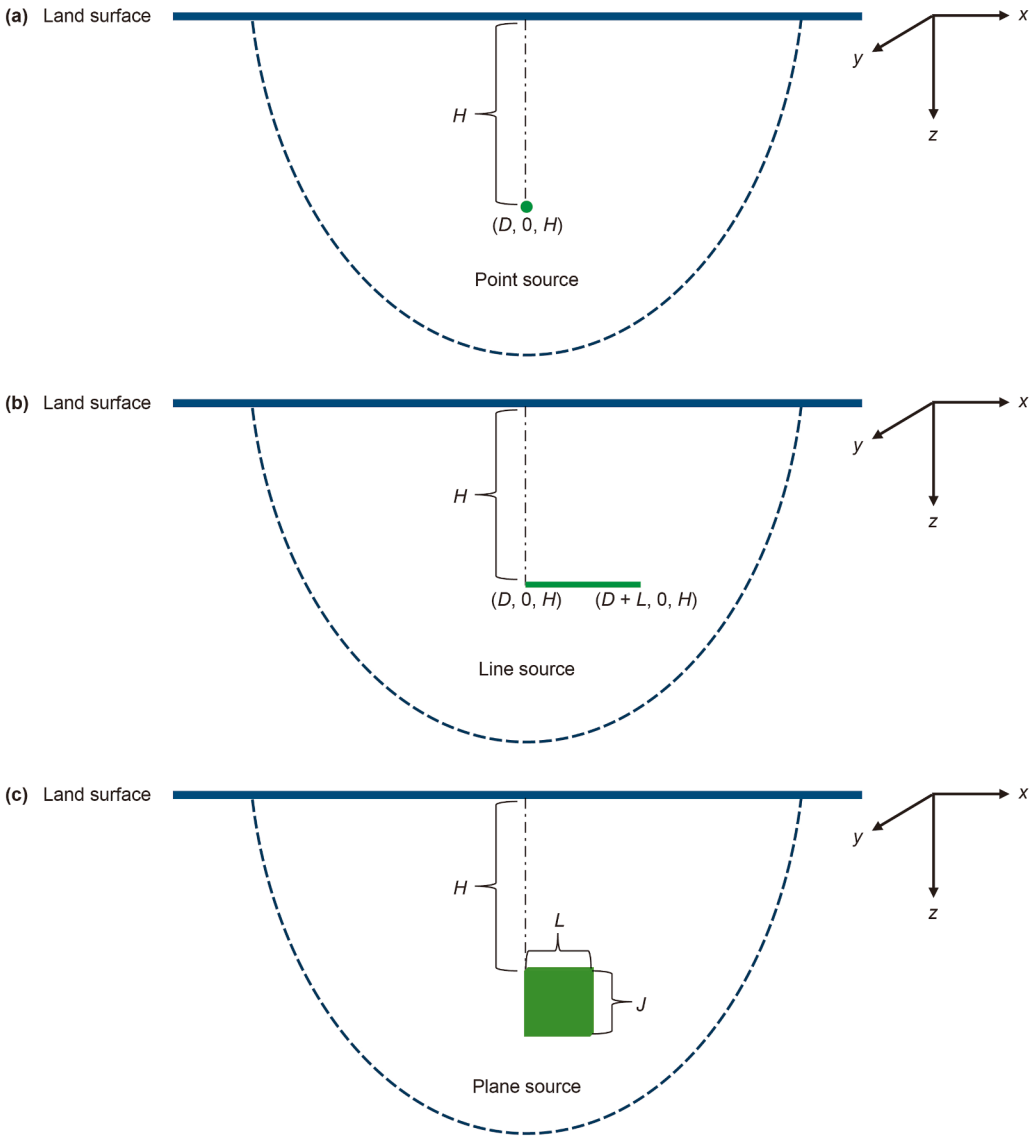

Fig. 1. (**a**) Conceptual model of a single point source locating at $(D, 0, H)$ in a half space. The green dot refers to the point source. (**b**) Conceptual model of a line source locating from $(D, 0, H)$ to $(D + L, 0, H)$. The green line refers to the line source. (**c**) Conceptual model of a plane source with the length of edge along the x and z directions being L and J. Geometrical parameters D, H, L, J are the horizontal position, depth, line length, and plane height, respectively.

reservoir with moderate depth and sandstone-rich shallow water reservoirs. Moreover, it is a common practice to assume the fluid flow to be single phase, otherwise analytical solution doesn't exist for the problem. For the boundary conditions, the problem is essentially free of vertical direction forces at the ground surface, as such it is traction-free at the top. Furthermore, the assumption of absence of surface supplemental flux leads to the no-flux boundary conditions. It should be noted such an assumption can be easily relaxed if any influx exists at the top. To incorporate the influx term, one only needs to add it to the solution of the fluid governing solution in the frequency domain, which will be shown in the methodology section. Except at the ground surface, the other directions are assumed to be unbounded, making the model a half space. The half-space domain is widely used in subsurface community (Rajapakse and Senjuntichai, 1993; Philippacopoulos, 1997; Lu and Hanyga, 2005), as the boundaries except the top surface of the field is difficult to locate. We will present the governing equation in the next sub-section.

2.2. Governing equations with boundary conditions

In this sub-section, we delineate the hydraulic and mechanical governing equations along with their boundary conditions. Under the assumptions described in the previous sub-section, the governing equations to be solved in this work are linear. Based on Biot's theory of incremental deformation (Biot and Romain, 1965), the fluid flow governing can be expressed as

$$\frac{\partial \zeta}{\partial t} = \frac{k}{\mu}\nabla^2 P + \xi \tag{1}$$

where ζ is the accumulation term considering the volumetric deformation of the liquid-rich rock; k and μ are the rock permeability and liquid viscosity, respectively; P and t are the pressure and time, respectively; ξ is the time-varying source term induced by the production. In this section, we first investigate the cases where ξ is the point source. We will show later that the solution of the line-source cases can be obtained easily based on the point-source solution using our approach. As a point source, ξ is then defined as $\xi = Q(t)\delta(D,0,H)$ where $Q(t)$ denotes the time-varying production history and $\delta(D,0,H)$ is the Dirac delta function (Jeffreys et al., 1956) with $(D,0,H)$ being the coordinate of the singular point, as shown in Fig. 1(a).

For the convenience of expression, we only solve for the case with one sink/source point in this work. The pressure and stress of cases with multiple sink/source points can be easily obtained by superposing the single-source solution, as described in elsewhere (Wang et al., 2023a). By substituting the definition of ζ (Jaeger et al., 2007) and q to Eq. (1), we get the following equation

$$\frac{\partial P}{\partial t} - M\alpha\frac{\partial \varepsilon_v}{\partial t} = \frac{kM}{\mu}\nabla^2 P + M\cdot\xi \tag{2}$$

where M, α, and ε_v are the Biot modulus, Biot coefficient, and volumetric strain, respectively.

Since in this work we target at the induced pressure-stress, which is essentially the 'change' of the variables, we need to eliminate the impact of the initial value of the primary variable by subtracting the initial value from Eq. (2), which yields the following equation.

$$s\overline{P} - M\alpha\overline{\varepsilon_v} = \frac{kM}{\mu}\left(\frac{\mathrm{d}^2\overline{P}}{\mathrm{d}z^2}(z,s) - q^2\overline{P}(z,s)\right) + M\overline{Q}(s)\mathrm{e}^{iq_xD}\delta(z-H) \tag{3}$$

where δP and $\delta\varepsilon_v$ are the variation of the pressure and the volumetric stress, respectively; s refers to the temporal variable yielded by Laplace transform. The above equation has the same formulation as Eq. (2), because the problem of interest is linear. Eq. (3) is the governing equation of the hydraulic process to be solved in this work. It needs to be mentioned that the initial values of the pressure and stress are fully determined by the boundary conditions and can be solved by the approach described in our previous work (Wang and Wu, 2022). The relationship between the Biot modulus and the compressibility is

$$M = \frac{1}{\phi c_f + (1-\phi)c_s - \frac{c_s}{1-\alpha}} \tag{4}$$

where ϕ, c_f and c_s are the rock porosity, fluid compressibility, and rock grain compressibility, respectively.

Next, we present the derivation of the mechanical governing equation. We start with the poroelastic constitutive relationship as below

$$\boldsymbol{\sigma} - \alpha P\boldsymbol{I} = 2G\boldsymbol{\varepsilon} + \lambda\varepsilon_v\boldsymbol{I} \tag{5}$$

where $\boldsymbol{\sigma}$ and $\boldsymbol{\varepsilon}$ are the stress and strain tensor, respectively; G and λ are the shear modulus and Lamé's first parameter, respectively; $\boldsymbol{I}$ is the unit tensor. Under the assumption of static equilibrium and ignoring the body force, the force equation is as follows:

$$\nabla\cdot\boldsymbol{\sigma} = 0 \tag{6}$$

Replacing the strain term with displacement yields the following Navier's equation for poroelastic materials.

$$(\lambda+G)\nabla(\nabla\cdot\boldsymbol{u}) + G\nabla^2\boldsymbol{u} + \alpha\nabla P = 0 \tag{7}$$

where $\boldsymbol{u} = [u_x, u_y, u_z]^{\mathrm{T}}$ is the displacement vector. In Eq. (7), the three displacement components are coupled with each other, making the solution derivation complex. To simplify the solution process, we introduce the 'mean stress' σ_m defined as $\sigma_m = (\sigma_{xx} + \sigma_{yy} + \sigma_{zz})/3$. The volumetric strain, the mean stress, and the pore pressure have the following relationship

$$\varepsilon_v = \frac{\sigma_m - \alpha P}{\lambda + \frac{2}{3}G} \tag{8}$$

With the introduction of the mean stress, Eq. (6) can be rewritten as

$$G\nabla^2\boldsymbol{u} + \frac{3}{2\nu+2}\nabla\sigma_m - \alpha\frac{1-2\nu}{2\nu+2}\nabla P = 0 \tag{9}$$

where ν is Poisson's ratio.

We will show later that the introduction of the mean stress is the key to simplifying the governing equations.

Eq. (9) is a vector-form equation set, which contains three components. Each component of the equation set consists of one displacement component, the mean stress, and the pressure. As such, we have 'decomposed' Eq. (7) to make it easier to solve. By differentiating each component of Eq. (9) with respect to x, y, and z, respectively, and adding up the resulted equations, we get the following 'mean stress' equation.

$$\nabla^2(\delta\sigma_m) = \alpha\frac{2(1-2\upsilon)}{3(1-\upsilon)}\nabla^2(\delta P) \tag{10}$$

The above equation only contains the mean stress and the pressure term. As such, if we could solve the pressure, we would solve the mean stress. Then using Eq. (8), we would solve all

displacement components. Eqs. (9) and (10) are thus used as the mechanical governing equations in this work.

While the governing equations are used to obtain the general solution of the pressure-stress fields, the boundary conditions fully determine the solution and are therefore indispensable. In what follows, we introduce the boundary conditions used in this work.

Firstly, the change of pressure at infinity ($z\to\infty$) should be zero and the fluid flux at the reservoir top surface should be zero as well. As such, the pressure change should satisfy the following boundary conditions.

$$\frac{\partial(\delta P)}{\partial z}(z=0)=0;\quad \delta P(z\to\infty)=0 \tag{11}$$

It should be mentioned that zero-pressure boundary conditions can also be handled by our method.

The displacement perturbation at infinity should be zero, as

$$\delta\boldsymbol{u}(z\to\infty)=0 \tag{12}$$

The top surface of the formation is traction-free, which implies that the z-direction traction forces (z-components of the stress tensor) should satisfy the following conditions

$$\delta\sigma_{zz}(z=0)=\delta\sigma_{xz}(z=0)=\delta\sigma_{yz}(z=0)=0 \tag{13}$$

From the physical perspective, the stress change at infinity should be bounded, as below

$$\delta\sigma(z\to\infty)<\infty \tag{14}$$

Next, we will show the derivation of the solution to the above governing equations.

2.3. Derivation of the fundamental solution

In this section, we present the process of deriving the fundamental solution. Our approach is inspired by previous works based on integral transform (Bufler, 1971; Cheng et al., 1991).

In this work, we use Laplace transform and Fourier transform to convert the governing partial differential equations (PDEs) to ordinary differential equations (ODEs) in the frequency domain. The detailed mathematical formulation of the two integral transforms can be found in Appendix A.

By applying Fourier transform to Eq. (3) along the x and y directions and applying Laplace transform in the time domain, we get the following equation

$$s\overline{P}=\frac{kM}{\mu}\left(\frac{\mathrm{d}^2\overline{P}}{\mathrm{d}z^2}(z,s)-q^2\overline{P}(z,s)\right)+M\overline{Q}(s)\mathrm{e}^{iq_xD}\delta(z-H) \tag{15}$$

where the superscript $^-$ denotes that the variable below is in the frequency domain; s refers to the temporal variable yielded by Laplace transform; q is defined as $q=\sqrt{q_x^2+q_y^2}$ where q_x and q_y are the frequency along the x and y directions, respectively; Q is the production rate (history).

To get the above equation, we have used the property of the Dirac delta function shown in Eq. (A-3). Similarly, by applying the same integral transform to Eqs. (9) and (10), we convert the mechanical governing equations to the frequency domain. Moreover, the primary variables of the mechanical governing equations can also be converted. The transformed formulations are listed in Appendix B.

To solve the transformed equations, we start with Eq. (B-4), which is a second order non-homogeneous ordinary differential equation (ODE) with the pressure-related term being the non-homogeneous part. The solution to this ODE consists of a general solution of the homogeneous part and a particular solution. The general solution is the linear combination of basis functions (exponential function in this case), while the particular solution can be guessed as the linear function of the pressure term. As such, the solution has the below formulation

$$\delta\overline{\sigma}_{\mathrm{m}}=a_1\mathrm{e}^{qz}+a_2\mathrm{e}^{-qz}+\alpha\frac{2(1-2\nu)}{3(1-\nu)}\delta\overline{P} \tag{16}$$

where $a_1(q,s)$ and $a_2(q,s)$ are unknown coefficients to be determined by the boundary conditions. It should be noted that, with fixed stress boundary conditions, $a_1=a_2=0$ and the mean stress is in linear relationship with the pressure changed, as proved in (Wang and Wu, 2022). The term $\alpha(2(1-2\nu)/3(1-\nu))$ is the 'depletion coefficient' commonly adopted in the geomechanics community (Jaeger et al., 2007). With the above relationship, the fluid flow governing equation is converted to the following equation,

$$\frac{\mathrm{d}^2(\delta\overline{P})}{\mathrm{d}z^2}(z,s)-m^2\delta\overline{P}(z,s)= -\frac{\mu}{k}\left(\frac{\alpha}{\lambda+\frac{2}{3}G}s\left(a_1\mathrm{e}^{qz}+a_2\mathrm{e}^{-qz}\right)-\overline{Q}(s)\mathrm{e}^{iq_xD}\delta(z-H)\right) \tag{17}$$

The term m is defined as

$$m^2=\frac{\mu}{kM}\left(s-\frac{M\alpha}{\lambda+\frac{2}{3}G}s\alpha\frac{2(1-2\nu)}{3(1-\nu)}+\frac{M\alpha^2}{\lambda+\frac{2}{3}G}s+\frac{kM}{\mu}q^2\right) \tag{18}$$

Moreover, it can be easily proved that m is not equal to q.

Therefore, the pressure solution is expressed as

$$\delta\overline{P}=\frac{1}{q^2-m^2}A_aa_2\mathrm{e}^{-qz}-\frac{1}{2m}\mathrm{e}^{-m|z-H|}A_Q\overline{Q} -\left(\frac{q}{m(q^2-m^2)}A_aa_2+\frac{1}{2m}A_Q\overline{Q}\mathrm{e}^{-mH}\right)\mathrm{e}^{-mz} \tag{19}$$

where A is defined in Eq. (C-1); a_2 is the only constant to be determined.

The solution of the above equation is shown with details in Appendix C. Once Eq. (19) is solved, we are allowed to solve Eq. (B-3) to get $\delta\overline{u}_z$. We first substitute Eqs. (16) and (19) into Eq. (B-3), then use the similar approach in solving Eq. (17), getting

$$\delta\overline{u}_z=-\frac{b_q}{2q}z\mathrm{e}^{-qz}+\frac{b_m}{m^2-q^2}\mathrm{e}^{-mz}-\frac{b_{|z-H|}}{q^2-m^2}\mathrm{e}^{-m|z-H|} \tag{20}$$

with

$$\begin{aligned} b_q&=qa_2\frac{3}{(2\nu+2)G}+\frac{q}{q^2-m^2}\alpha\frac{1-2\nu}{2(1-\nu)G}A_aa_2\\ b_m&=-\alpha\frac{1-2\nu}{2(1-\nu)G}\left(\frac{q}{(q^2-m^2)}A_aa_2+\frac{1}{2}A_Q\overline{Q}\mathrm{e}^{-mH}\right)\\ b_{|z-H|}&=-\alpha\frac{1-2\nu}{4(1-\nu)G}A_Q\overline{Q}\frac{z-H}{|z-H|} \end{aligned} \tag{21}$$

Similarly, $\delta\overline{u}_x$ and $\delta\overline{u}_y$ can be solved as

$$\begin{aligned}\delta\overline{u}_x=&\frac{1}{2q}\left(a_2 iq_x\frac{3}{(2\nu+2)G}+\frac{1}{q^2-m^2}A_a a_2\right)z\mathrm{e}^{-qz}\\&-\frac{1}{2m}\frac{A_Q\overline{Q}}{q^2-m^2}\mathrm{e}^{-m|z-H|}\\&+\left(\frac{q}{m(q^2-m^2)}A_a a_2+\frac{1}{2m}A_Q\overline{Q}\mathrm{e}^{-mH}\right)\frac{1}{m^2-q^2}\mathrm{e}^{-mz}\end{aligned}\tag{22}$$

$$\begin{aligned}\delta\overline{u}_y=&\frac{1}{2q}\left(a_2 iq_y\frac{3}{(2\nu+2)G}+\frac{1}{q^2-m^2}A_a a_2\right)z\mathrm{e}^{-qz}\\&-\frac{1}{2m}\frac{A_Q\overline{Q}}{q^2-m^2}\mathrm{e}^{-m|z-H|}\\&+\left(\frac{q}{m(q^2-m^2)}A_a a_2+\frac{1}{2m}A_Q\overline{Q}\mathrm{e}^{-mH}\right)\frac{1}{m^2-q^2}\mathrm{e}^{-mz}\end{aligned}\tag{23}$$

Then by substituting the expressions in Eqs. (16), (19) and (20) into Eq. (B-7), and enforcing the traction free boundary condition at the top surface, we can solve a_2 as

$$a_2=\frac{2\mu q^2(1+\nu)(q^2-m^2)E\alpha\mathrm{e}^{-mH+iq_xD}\overline{Q}}{-3\left[m(q^2-m^2)(q^2-m^2)\right](1-\nu)kE+3\mu\alpha^2 s[1-2\nu]\{m(q^2-m^2)(3\nu-1)+2q^3(1+\nu)\}}\tag{24}$$

where E is the Young's modulus.

By substituting the above formulation into Eqs. (20)–(23), we can obtain the explicit formulations of the displacement components. Then by substituting the displacement formulations into the stress formulations in Eqs. (B-5) to (B-10), we get the formulations of all stress components in the Fourier–Laplace domain. We list out their detailed formulations in Appendix D, along with a flowchart diagram showing the steps of the whole derivation.

By applying the inverse integral transforms described in Appendix A, we will get the solution of the displacement as well as the stress components in the original domain. As such, the fundamental solution is fully obtained. Now that we have obtained the point source solution, we will present the derivation of the line source and plane source solution in the next sub-section, in order to extend the model to horizontal wells and fractures.

2.4. Line source and plane source solution

Since our analytical solution solely consists of elementary functions in the Fourier–Laplace domain, it can be easily extended to the line source and plane source solution, which is one of the novelties of this work.

We first describe the extension to the line source solution. Considering a line source lying along the y axis between point (D, 0, H) and ($D+L$, 0, H) as shown in Fig. 1(b), the line source solution can be determined by integrating the point source solution. The results can be simply obtained by replacing all e^{iq_xD} terms with $\left(\mathrm{e}^{iq_x(D+L)}-\mathrm{e}^{iq_xD}\right)/iq_x$ and multiplying all terms without e^{iq_xD} by L. For instance, the line source solution of the pressure in the Fourier–Laplace domain is calculated as follows:

$$\delta\overline{P}_l(z,s)=\int_D^{D+L}\delta\overline{P}(z,s)\mathrm{d}x\tag{25}$$

Using the above approach, the line source solution of the displacement as well as stress can be obtained similarly. The detailed formulations are abbreviated in this work for simplicity.

The plane source solution can be obtained using a similar approach to the line source solution. If the length of the plane source along the z direction is J, as shown in Fig. 1(c), then the plane source solution of the pressure field can be calculated based on the line source solution using the following formulation.

$$\delta\overline{P}_p(z,s)=\int_H^{H+J}\delta\overline{P}_l(z,s)\mathrm{d}x\tag{26}$$

The results can be expressed by replacing all e^{-mH} terms in the line source solution by $\left(\mathrm{e}^{-m(H+J)}-\mathrm{e}^{-mH}\right)/(-m)$ and multiplying all terms without e^{-mH} by J.

As such, we have obtained the line and plane source solution in close-form in the Fourier–Laplace domain. Compared with previous work (Rajapakse and Senjuntichai, 1993; Jin and Liu, 2001) that require numerical integral operations, our method is clearly more efficient. The above is the completed derivations of the point source, line source and plane source solutions. In the next sections, we will present the validation of the solutions.

3. Validation

In this section, we validate the derived solution by comparing with both existing analytical solutions and an in-house finite element program (Wang et al., 2024). We compare our model with Rajapakse's analytical solution for the special case of a point source solution. Moreover, we compare the line source solution with the finite element program, which conducts coupled hydraulic-mechanical simulation of poroelastic reservoirs. Based on published works, the numerical program has been validated with respect to classical analytical solutions as well as field observations (Khebzegga et al., 2022; Wang et al., 2022a; Wu et al., 2022). Therefore, it is a trustful program for validating the newly derived solution. For the sake of convenience, we ignore the fluid compressibility in Eq. (4), so that the rock compressibility is fully determined by the Biot modulus and the rock porosity. In the unit conversion session at the end of this paper, we list out the converting factor between the field units to SI units.

3.1. Validation of the point source solution

In this sub-section, we first validate the point source solution by mimicking the point source as a production well. Meanwhile, we aim to investigate the impact of the traction-free boundary on the pressure–stress distribution. Since this is an axially symmetric case, we can directly compare our solution with both Rajapakse's analytical solution and FEM solution. A point source is placed at the center of the x–y plane within the cubic reservoir. To keep the validation section concise, we only present the comparison with Rajapakse's analytical solution in this sub-section and save the comparison with the numerical program along with analysis of the boundary effect in Section 4.1. A conceptual model of the system is shown in Fig. 2. The rock and fluid parameters used for the validation are listed in Table 1.

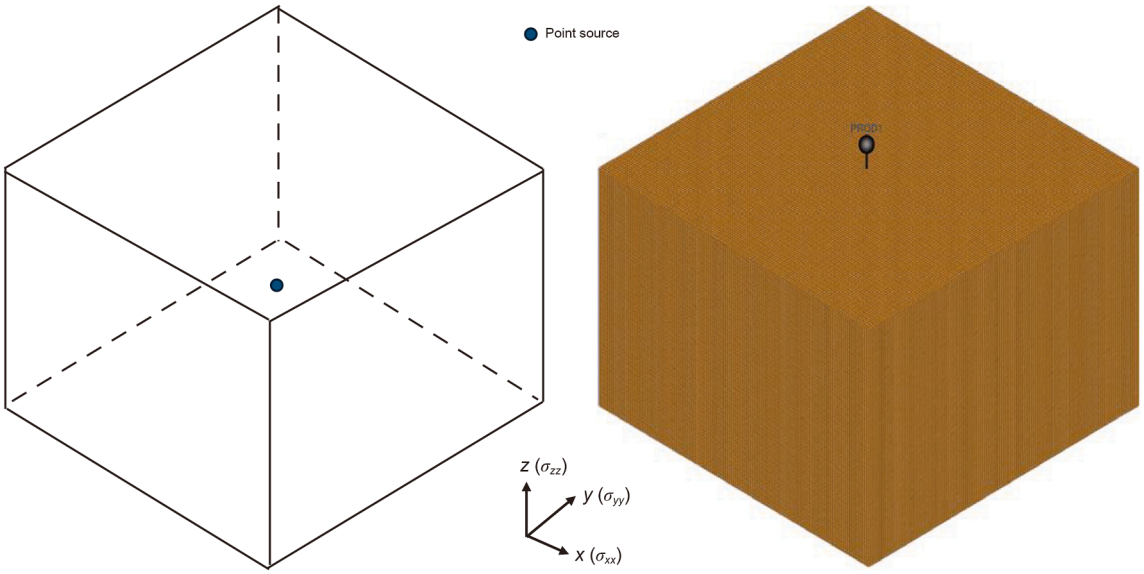

Fig. 2. Grid system of the numerical model for the FEM program.

Table 1
Input parameters of the validation case for the point source solution.

Parameters	Values	Units
Rock permeability k	1	mD
Rock porosity ϕ	0.15	Dimensionless
Poisson's ratio ν	0.1	Dimensionless
Biot's coefficient α	0.7	Dimensionless
Biot's modulus M	1.1×10^6	psi
Young's modulus E	3.5×10^6	psi
Liquid viscosity μ	1.0	cP
Liquid density ρ	62	lbm/ft^3
Liquid production rate Q	1	bbl/d/well
Production duration t	60	d

To compare with Rajapakse's analytical result, we set the point source 65 ft below the ground surface. When running our model, we truncate the integral transform by 150 terms. Fig. 3 compares the $\delta\sigma_{xx}$ profile along the z direction obtained by our solution and Rajapakse's solution. It can be seen that the two methods yield close results in this case study. This implies that our solution is able to reproduce the axially symmetric results from classical analytical solutions. In Section 4.1, we further compare our results with a numerical program.

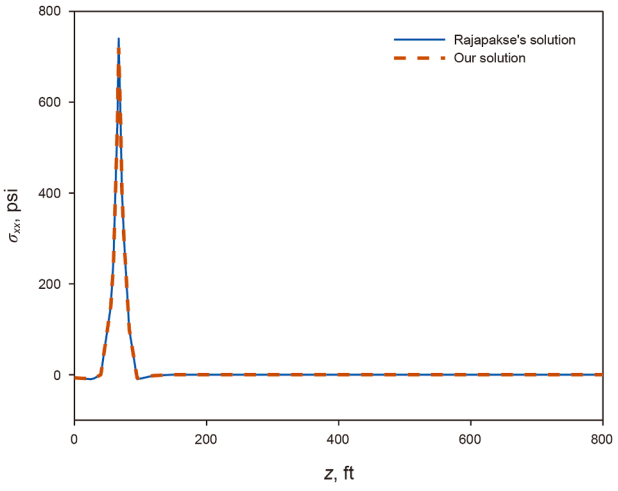

Fig. 3. Comparison of normal stress along the z direction between Rajapakse's solution and our solution for a point source case.

3.2. Validation of the line source solution

In this sub-section, we present a validation case for the proposed line source solution using the same model setup shown in the previous sub-section. In this case, we deal with a 300 ft-long line source along the x direction at a depth of 150 ft. We set observation points A and B, which are the projection of the middle point and ending points of the line source on the surface plane, as shown in the upper part of Fig. 4. The input parameters used for this case are listed in Table 2.

We will compare the induced normal stress within the x–z plane in which the line source locates, and the time-varying surface subsidence at the observation points during the production. The normal stress profiles yielded by the analytical solution and the numerical program are shown in the lower left and lower right of Fig. 4, respectively. It can be seen that the line source creates a stress concentration region beneath it, while there is no stress concentration at the top surface due to the effect of the traction-free surface.

The surface subsidence (reverse z-direction displacement) at observation points A and B is compared in Fig. 5. Upon comparison, our derived solution is very close to the numerical results. The average difference of the stress value and the subsidence is both below 4%. In this sense, the line source solution is validated.

3.3. Validation of neighboring wells with TOUGH-FLAC

In this case study, we compare the developed semi-analytical solution with a widely adopted numerical program, namely TOUGH-FLAC, to benchmark the solution. TOUGH-FLAC (Rutqvist, 2011) couples the multiphase fluid flow capabilities of TOUGH2 (Pruess, 1991) with the geomechanics of FLAC3D to simulate complex thermal-hydrological-mechanical (THM) processes in geological media. Its core strength lies in a sequential coupling scheme where pore pressure and temperature changes drive mechanical deformation, which then feeds back to dynamically update hydraulic properties like porosity and permeability. The

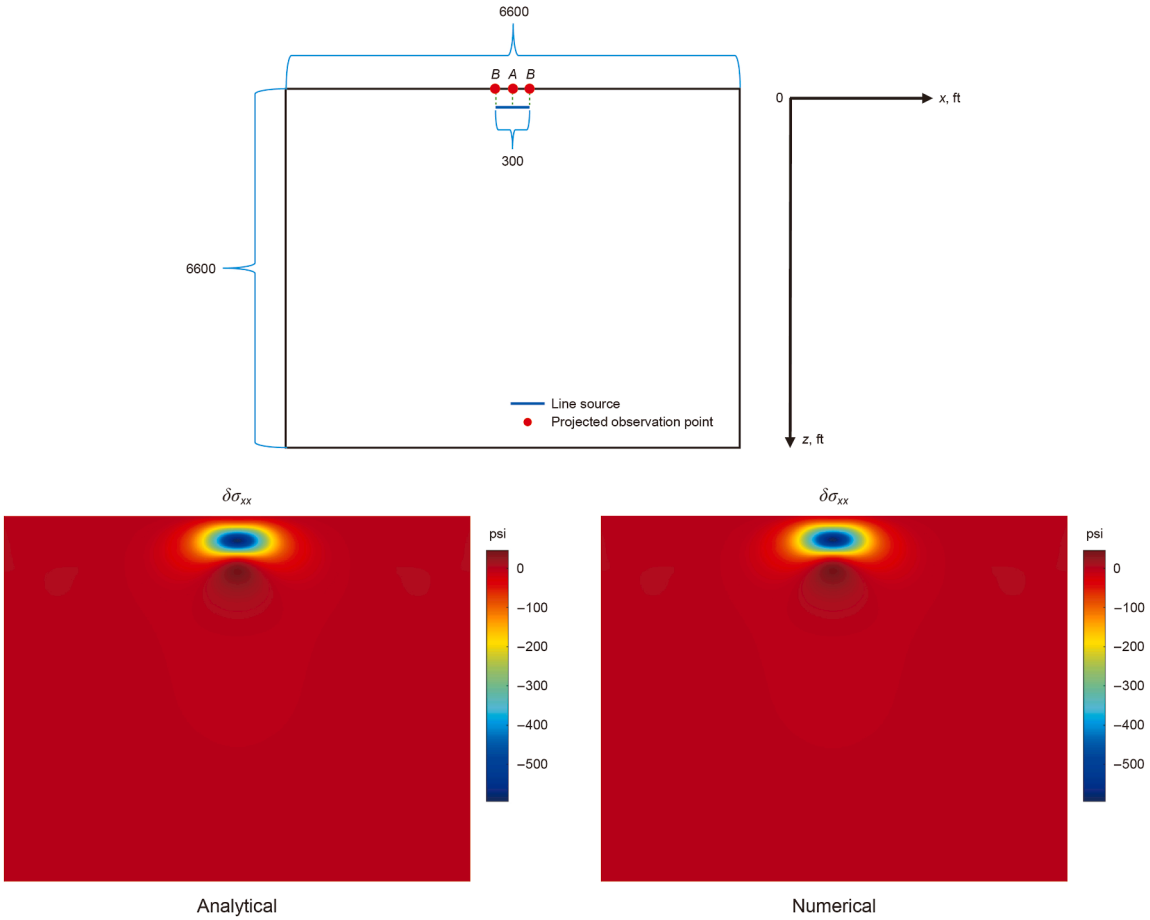

Fig. 4. Upper: conceptual model of the line source validation case. Lower left: $\delta\sigma_{xx}$ profile calculated by the proposed analytical solution. Lower right: $\delta\sigma_{xx}$ profile simulated by the FEM program.

program has been widely used in the simulation of geothermal reservoirs, carbon sequestration problems and ground water reservoirs.

We set up a case study in which two parallel line sources mimicking a pair of horizontal wells locate in the center of a reservoir. The size of the reservoir is 1600 ft × 1600 ft × 1600 ft, which is large enough for the boundary effect in the horizontal direction to vanish. The length of each horizontal well is 250 ft. The distance between of them is 350 ft. The TOUGH-FLAC simulation requires the computational domain to be discretized. To balance speed and accuracy, we have adopted a local refinement strategy. We use a nested grid system. In the 800 ft × 800 ft × 800 ft cube that locates in the center of the model, we use a refined mesh in which each grid block is 20 ft × 20 ft × 20. In the rest of the system,

Table 2
Input parameters of the validation case for the line source solution.

Parameters	Values	Units
Rock permeability k	0.4	mD
Rock porosity ϕ	0.1	Dimensionless
Poisson's ratio ν	0.15	Dimensionless
Biot's coefficient α	0.8	Dimensionless
Biot's modulus M	1.0×10^6	psi
Young's modulus E	3.5×10^6	psi
Liquid viscosity μ	0.9	cP
Liquid density ρ	62	lbm/ft^3
Liquid production rate Q	20	bbl/d/well
Production duration t	100	d

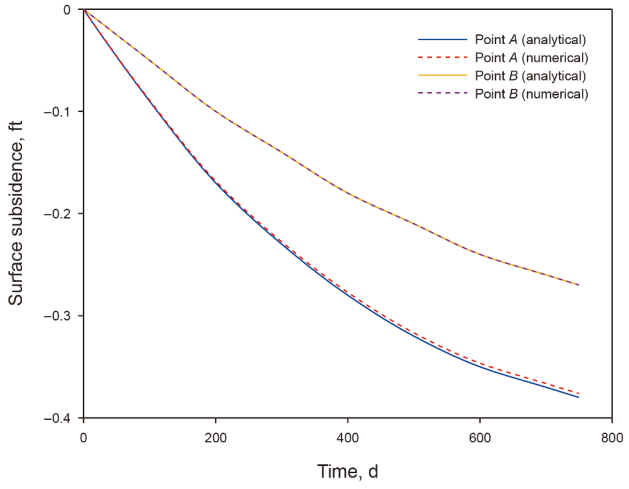

Fig. 5. Comparison of the time-varying subsidence at observation points *A* and *B*.

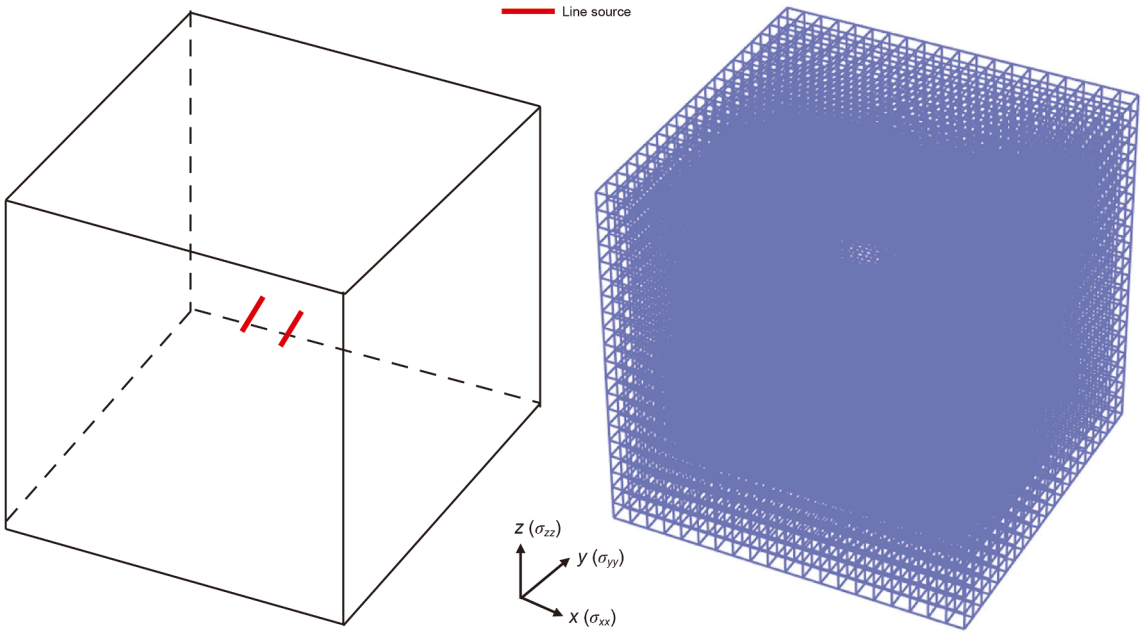

Fig. 6. Left: conceptual model of a large cubic reservoir with two horizontal wells in the center. Right: mesh system used for the simulation.

Table 3
Input parameters for the case of neighboring well.

Parameters	Values	Units
Rock permeability k	0.2	mD
Rock porosity ϕ	0.12	Dimensionless
Poisson's ratio ν	0.1	Dimensionless
Biot's coefficient α	0.7	Dimensionless
Biot's modulus M	1.0×10^6	psi
Young's modulus E	4.5×10^6	psi
Liquid viscosity μ	0.8	cP
Liquid density ρ	60	lbm/ft^3
Liquid production rate Q	50	bbl/d/well
Production duration t	30	d

we use a coarser grid in which each grid block is 80 ft $\times$ 80 ft $\times$ 80 ft. The conceptual model and the mesh grid of this case is shown are shown in the left and right of Fig. 6, respectively. The other input parameters are listed in Table 3.

We compare the spatial distribution of pressure and stress change (σ_{xx}, σ_{yy}) calculated by the numerical program and the semi-analytical solution on the horizontal plane that cuts through the two horizontal wells. The results are presented in Figs. 7 and 8. As indicated by the comparison, our solution precisely reproduces the numerical results. The average difference is below 3%. This comparative study further validates the accuracy of our model. Moreover, according to the results, the stress change propagates much farther than the pressure change. We will further investigate this phenomenon in Section 4.

4. Application

In this section, we apply the derived analytical solution to three case studies to demonstrate the feasibility of the solution.

4.1. Boundary effect on induced stress

As mentioned in Section 3, we use the developed model to investigate the impact of the traction-free surface on the induced stress, and compare the results with a FEM program. The model setup along with input parameters have been described in Section 3.1. To model a semi-infinite reservoir using the FEM program, we build a model with a cubic shape and discretize it into 151 $\times$ 151 $\times$ 151 grid blocks. The side length of each grid block is 8 ft. In the numerical model, the top of the cube is set as traction-free boundary while the other boundaries are with (fixed) zero displacements. Via several trial runs, we confirm that the model is large enough that the zero displacement has negligible impacts on the stress distribution in the vicinity of the point source. In this case, we investigate the pressure and stress responses when the point source locates at the depth of 84 and 524 ft.

Figs. 9 and 10 show the results regarding the case where the point source is located at 84 ft in depth. According to the figures, the magnitude of the stress change above the point source is smaller than that below it. This is because that the traction-free boundary alters the stress profile near the surface. In contrast, the pressure profiles above and below the point source demonstrate less difference. This is due to the fact that the stress change normally has a broader range of impact compare the pressure change (Wang et al., 2023a). As such, the top boundary has less impact on the pressure than on the stress.

Figs. 11 and 12 show the results of the case where the point source is located at 524 ft in depth. From the plots it can be seen that the stress and pressure profiles above and below the point source in this case are almost identical. This is because when the point source is deep enough, the impact of the traction-free boundary is no more significant. The impact of the top surface can be quantitatively understood through the quantitative analysis of the mathematical structure of the solution. As discussed in the

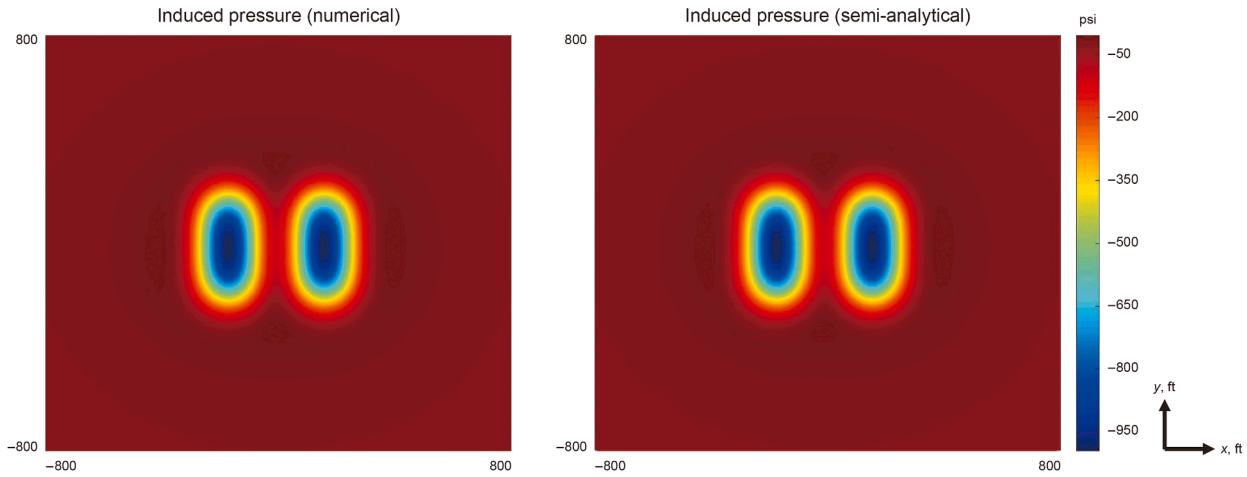

Fig. 7. Comparison of the pressure fields yielded by the numerical simulator and the semi-analytical solution on the plane at the middle of the model.

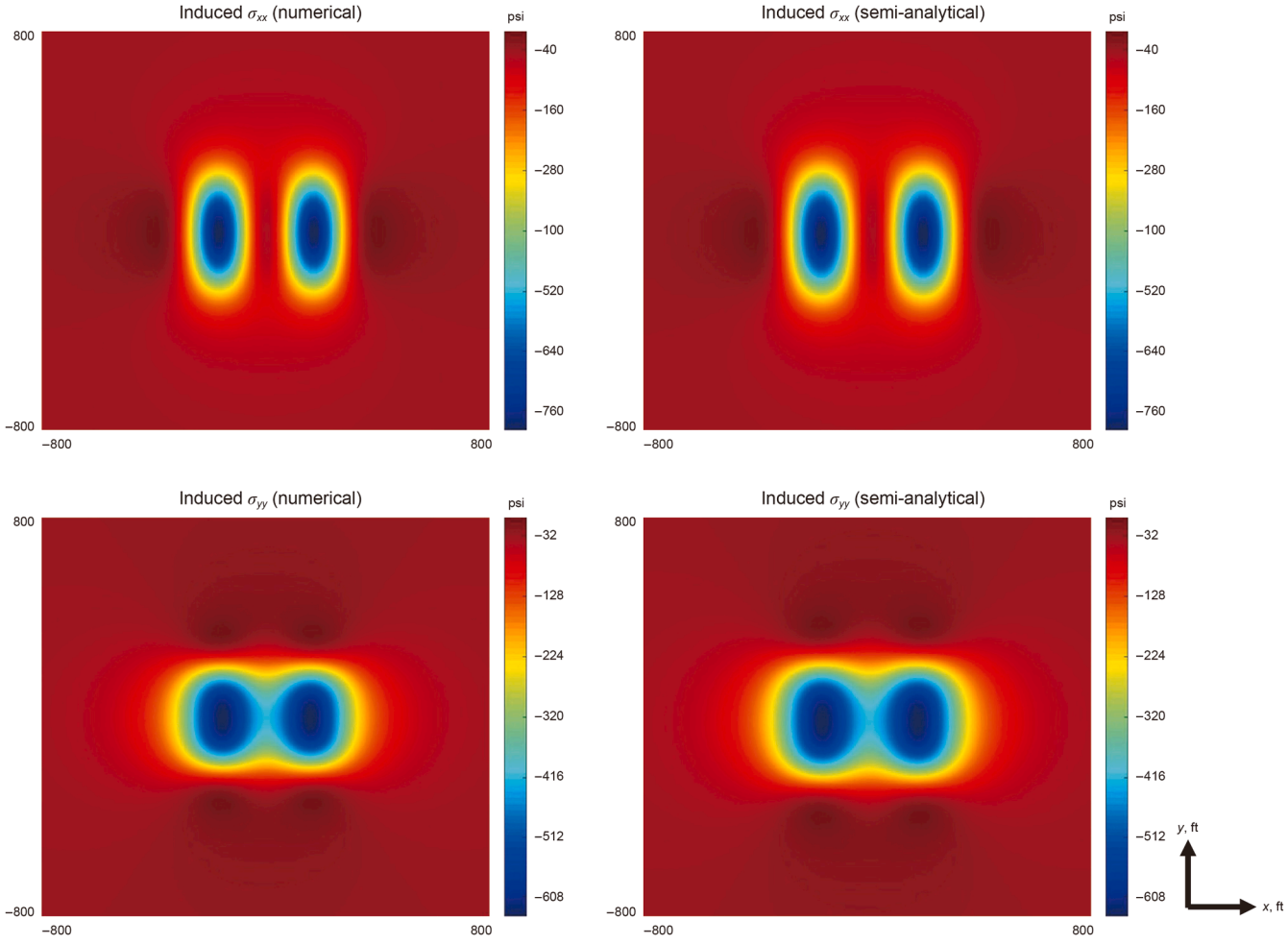

Fig. 8. Comparison of the pressure fields yielded by the numerical simulator and the semi-analytical solution on the plane at the middle of the model.

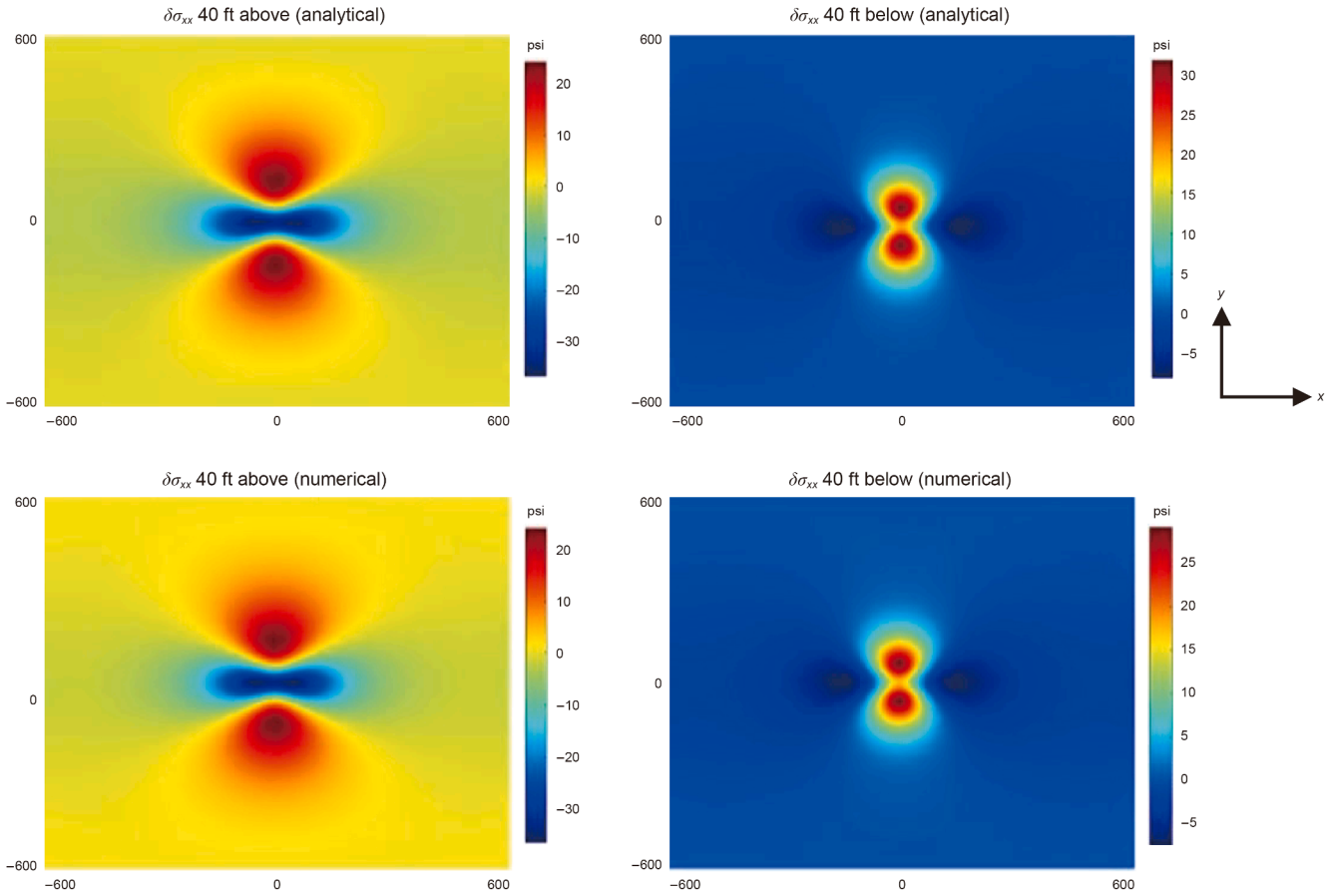

Fig. 9. $\delta\sigma_{xx}$ profile (top view) at observation point 40 ft above and below a production point locating at a depth of 84 ft.

previous section, the traction-free surface results in the non-homogeneous term in Eq. (19), which contains the exponential function. Therefore, when the depth increases, the impact of the traction-free surface declines sharply. This is consistent with our previous findings in elsewhere (Wang et al., 2022b).

According to the above-mentioned four figures, our analytical solution matches well with the numerical program. The average difference between the results yielded by the two approaches is below 3%. In each case, it takes more than 20 min for the numerical program to complete the simulation on 32 processors, while the analytical solution spends less than 14 s on a single CPU. As such, the proposed analytical solution outperforms the numerical program in computational efficiency while preserving accuracy.

4.2. Surface subsidence control

In this sub-section, we apply the derived analytical solution to a synthetic case study about the surface subsidence control. We consider a shallow water reservoir in which two parallel horizontal wells are set to produce for 1 year. The depth of the wells is 50 ft to the top surface. The extraction of subsurface liquids causes the ground surface to subside. A third horizontal well is then drilled to inject fluids into the formation for the purpose of pressure maintenance and subsidence remedy. We assume that the injection well is in the same depth of the production well. Regardless of any economic considerations, we aim to optimize the length of the injection well by minimizing the maximum value of the induced surface movement ($\max|\delta \boldsymbol{u}_z|$). The input parameters used in this case are listed in Table 4. A bird view of the plane at which the horizontal wells are located is shown in the left of Fig. 13, while the surface movement at the end of the production is shown in the right of Fig. 13.

As the results, the surface displacement profiles with respect to different length of the injection well are shown in Fig. 14. Clearly, when the injection well is very short, its hydraulic-mechanical behavior is similar to a point source. In this sense, the injected fluids will accumulate in the vicinity of the wellbore and the pressure increment doesn't have enough time to propagate to the depleted zone. This will lead to the upward movement of the ground surface along the injection well, while the ground surface above the production wells remains to be subsiding. In contrast, when the injection is too long, the pressure drawdown induced by its unit length will be very small. Under this condition, the injection well cannot help remedy the subsidence.

4.3. Stress interference between two horizontal wells

In this sub-section, we study one case regarding the stress interference between two neighboring fractured wells using the plane source solution. In this case, two horizontal wells with zipper-type fractures lying 200 ft away from each other are drilled in a tight oil reservoir. Each horizontal well has five fractures, among which the fracture spacing is 100 ft. In each horizontal well, the half-length of the two outer fractures is set as 150 ft while the half-length of the three fractures in the middle is assumed to be 100 ft. The fractures tips from the two wells are close to each other,

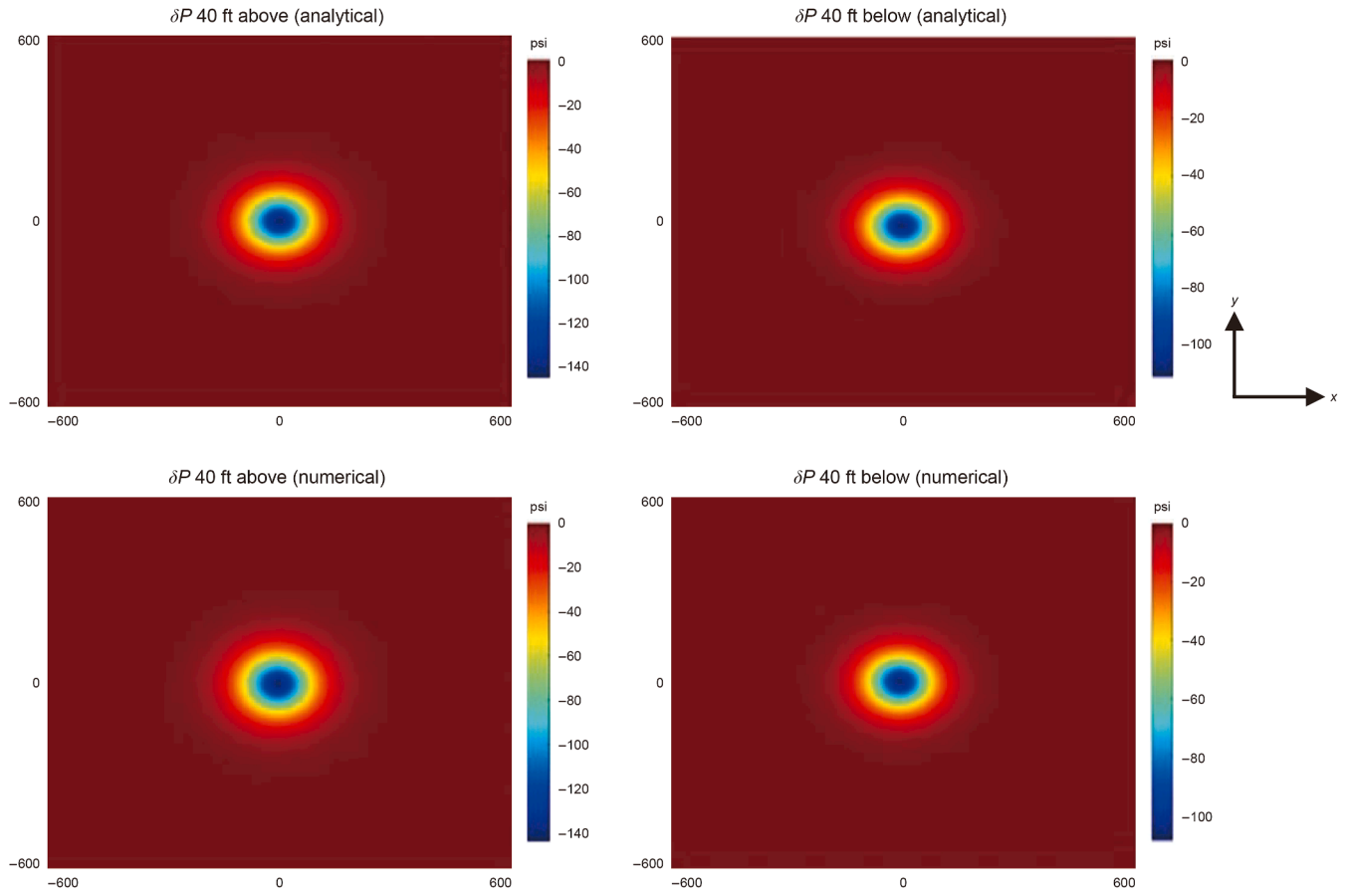

Fig. 10. δP profile (top view) at observation point 40 ft above and below a production point locating at a depth of 84 ft.

to mimic the parent-child well pairs. The bird view of the two horizontal wells with the fractures is shown in Fig. 15. The parameters used in this case study are listed in Table 5. To understand the impact of rock permeability on the stress variation, we run a high-permeability case and a low-permeability case. In the former case, the rock permeability is set as 10 μD, while in the latter case the rock permeability is 3 μD.

As the results, the variation of pressure (δP), normal stress ($\delta\sigma_{xx}$, $\delta\sigma_{yy}$), and shear stress ($\delta\sigma_{xy}$) at the layer of production for the low-permeability case and the high-permeability case are compared in Figs. 16 and 17, respectively. According to the comparison, given the same amount of produced fluids, the low-permeability yields higher pressure reduction in the vicinity of the fractures. The sharp decline of pressure further results in large stress reduction. As such, low-permeability reservoirs in general are more sensitive to production-induced hydraulic-mechanical permutations. Moreover, it is interesting to see that the shear stress is not changed much in the region where fractures of the wells are close to each other. We call this region the 'fracture-crossing region'. Although the stress interference from the normal stress is high in the 'fracture-crossing region', the shear stress interference in the same region is not significant. This is because that the fractures in this work are parallel to each other, and the shear stress induced by one fracture will be compensated by its neighboring fracturs.

The production will also induce the reorientation of the principal stress. To examine the stress reorientation effect, we compare the direction of the maximum horizontal stress of the two cases in Figs. 18 and 19. The direction of the 3D principal stress fields is computed using the formulation provided by Jaeger et al. (2007). Since the stress reorientation effect mostly impacts the fracture propagation of neighboring wells, we only plot the stress direction within the fracture tip region, of which both x and y coordinates are between 800 and 1200. According to the figures, the principal stress is not significantly altered in the fracture-crossing region of the high-perm case. This is because the shear stress change in this region is small, as discussed in the previous paragraph. Based on the formulation of the stress angle, the reorientation effect in this region is thus relatively smaller. Meanwhile, the stress direction change spans to a wider range in the high-permeability case due to the pressure diffusion, indicating that the stress alteration affects wells that are farther away in reservoirs with higher permeability. This cases shows that our solution has potential implications on the fracture driven interaction (FDI) study (Scherz et al., 2020). This completes the case studies. In the next sections we will present the summary and conclusions.

5. Summary

To sum up, we have developed an analytical solution to the coupled hydraulic-mechanical problems in semi-infinite isotropic poroelastic reservoirs. Our solution is based on integral transforms and can be naturally extended to line source and plane source scenarios. We have brought out a novel approach to convert the governing PDE into a series of ODEs in the frequency domain. The benchmarking of the solution, with respect to both analytical solution and open-source numerical programs, demonstrates its

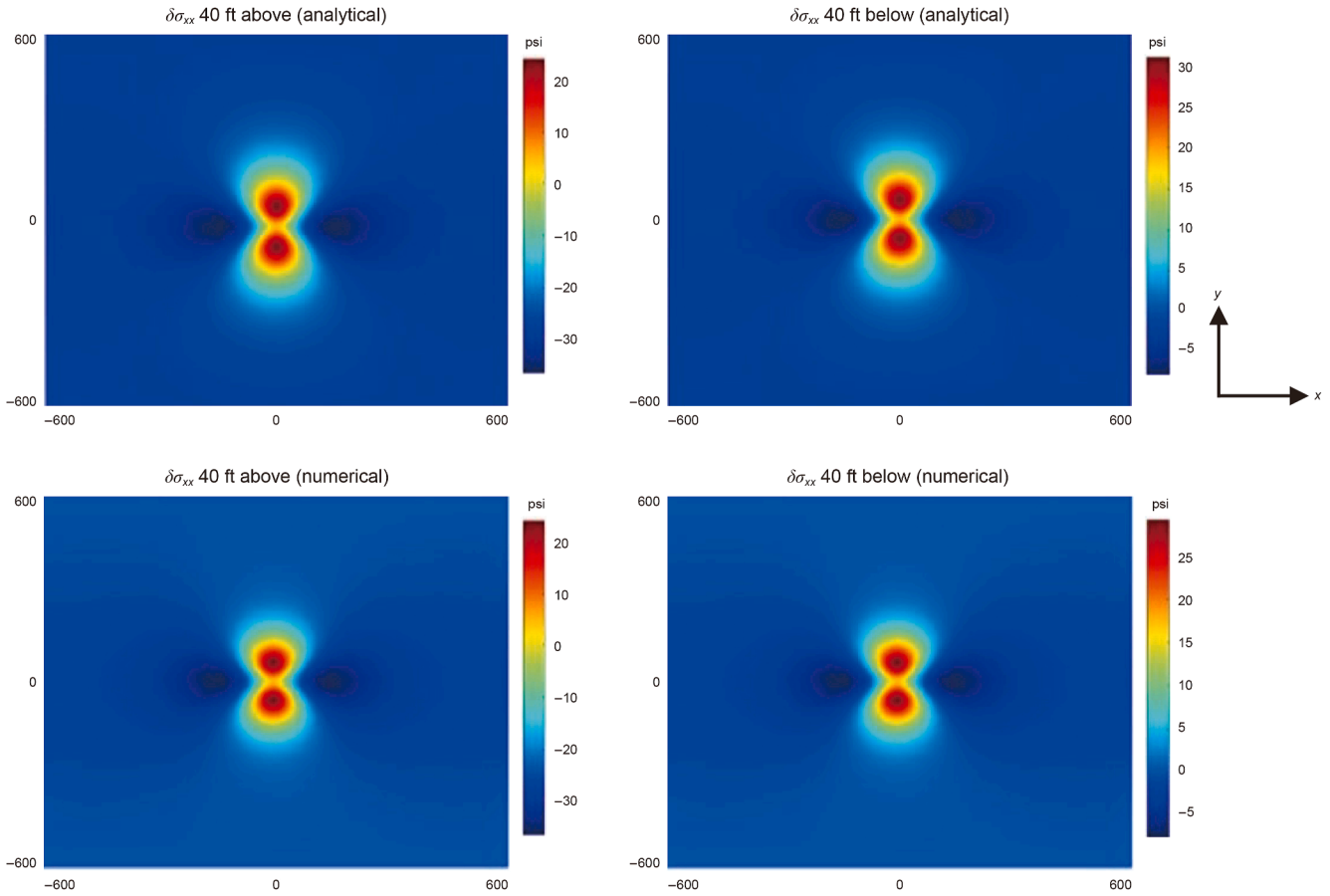

Fig. 11. $\delta\sigma_{xx}$ profile (top view) at observation point 40 ft above and below a production point locating at a depth of 524 ft.

accuracy. We have applied the derived solution to investigate the surface subsidence and stress interference problems. In the case study, we have demonstrated that the solution is effective in capturing the stress re-orientation between neighboring fractured wells, which sheds light on the optimization of drilling plans in area with close well spacing. Compared to numerical program, the solution is significantly more efficient, which enables to be applied to field-scale operations with multiple wells. Beyond its theoretical novelty, the solution offers practical extensibility to various source geometries and provides critical insights into geomechanical phenomena, specifically surface subsidence and stress interference in reservoir engineering. Next we conclude the work through the discussion of the strength and limitations of the model.

Table 4
Input parameters of the subsidence case study.

Parameters	Values	Units
Rock permeability k	0.9	mD
Rock porosity ϕ	0.14	Dimensionless
Poisson's ratio ν	0.1	Dimensionless
Biot's coefficient α	0.9	Dimensionless
Biot's modulus M	1.0×10^6	psi
Young's modulus E	3.0×10^6	psi
Liquid viscosity μ	0.7	cP
Liquid density ρ	60	lbm/ft^3
Liquid production rate Q	150	bbl/d/well
Production duration t	360	d

6. Discussion

We believe the solution will have wide applications in the modeling of petroleum as well as groundwater reservoirs. Moreover, this solution along its novel treatment to the mechanical boundary lays the foundation for the derivation of hydraulic-mechanical solutions of multilayer problems (Xiao et al., 2019). In multilayer problems, the boundary conditions on the interface between two neighboring layers should ensure the continuity of flow and traction. The pressure, flux, displacement as well as z-related stress tensor components should be continuous across the layer interfaces. Therefore, the solution procedure is similar to what is proposed in this work, that upon integral transform the problem becomes a linear system. As such, our model serves as the 'first' and the 'last' layer in the multilayer cases. The actual challenge in multilayer problems lies in the numerical stability in solving the linear system due to its high condition number. Certain strategies, such as the propagator matrix method (Alshits et al., 2001) and the flexibility matrix method (Peirce and Siebrits, 2001), have been proposed to address the issue. So far multilayer analytical models for coupled hydraulic-mechanical processes are

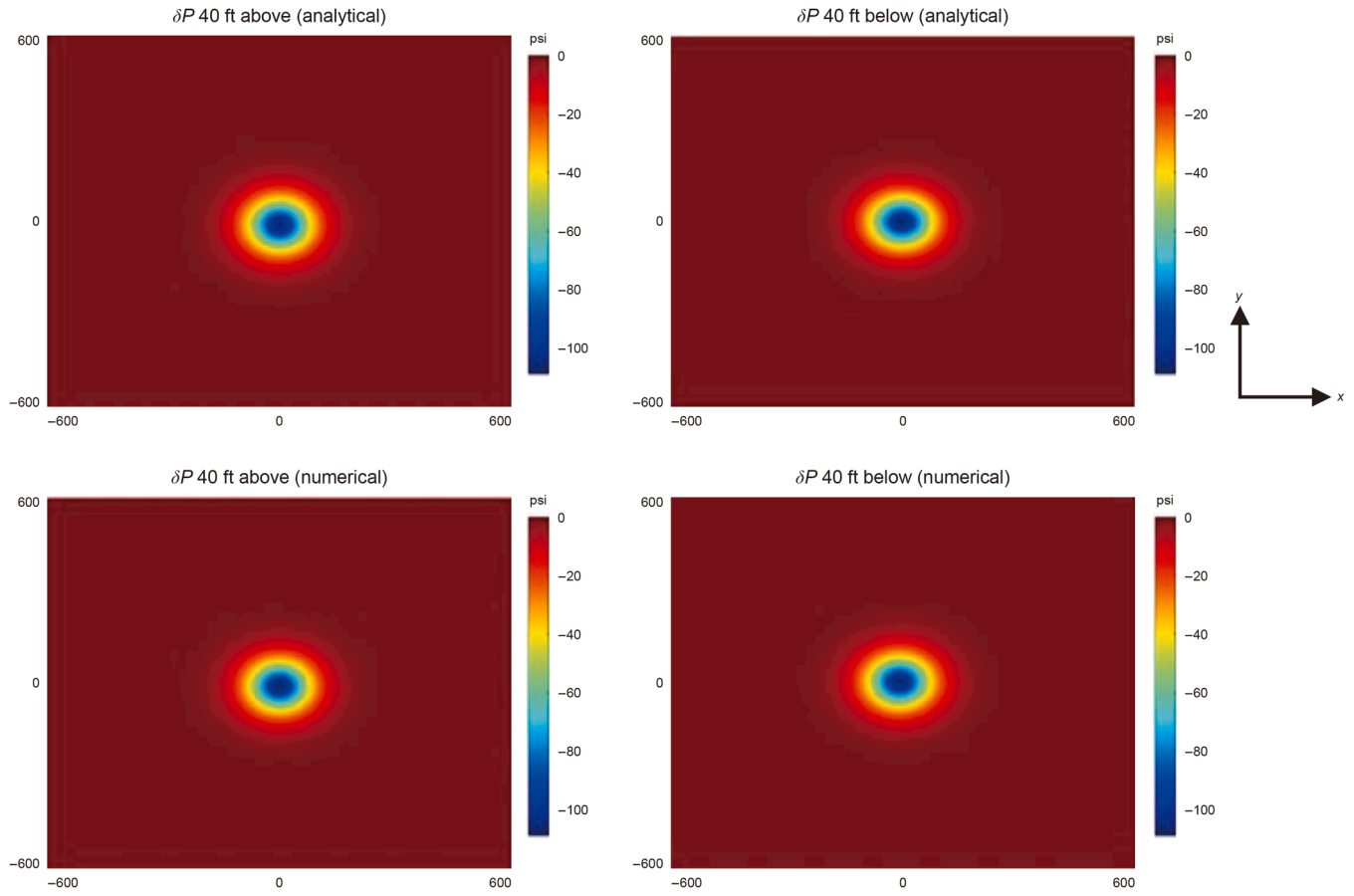

Fig. 12. δP profile (top view) at observation point 40 ft above and below a production point locating at a depth of 524 ft.

lacking and it is our ongoing efforts to derive such a model with sound robustness. Additionally, our model can also be extended to include the nonlinear compaction effect of fractures. Since our model is essentially a fundamental solution of the pressure-stress response subject to the extraction of unit amount of fluids from the reservoir, it can be combined with the approach proposed by (Zhou et al., 2013) to formulate a semi-analytical method with the consideration of finite fracture permeability. Zhou's method is essentially a numerical simulator of the fracture system with the fluid flow inside the matrix obtained from an analytical solution.

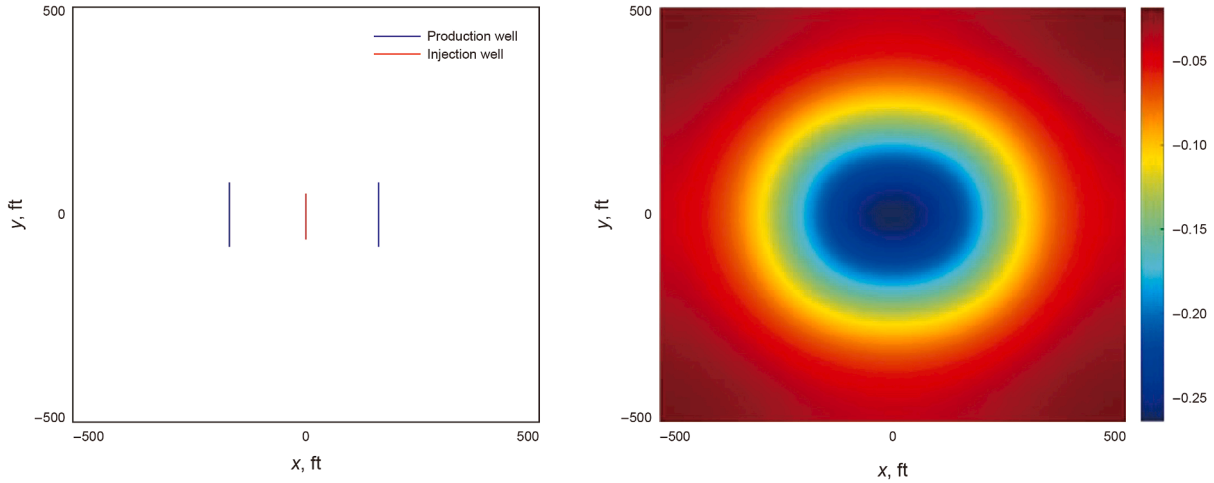

Fig. 13. Left: conceptual model of the production and injection wells. Right: surface subsidence after one year of production.

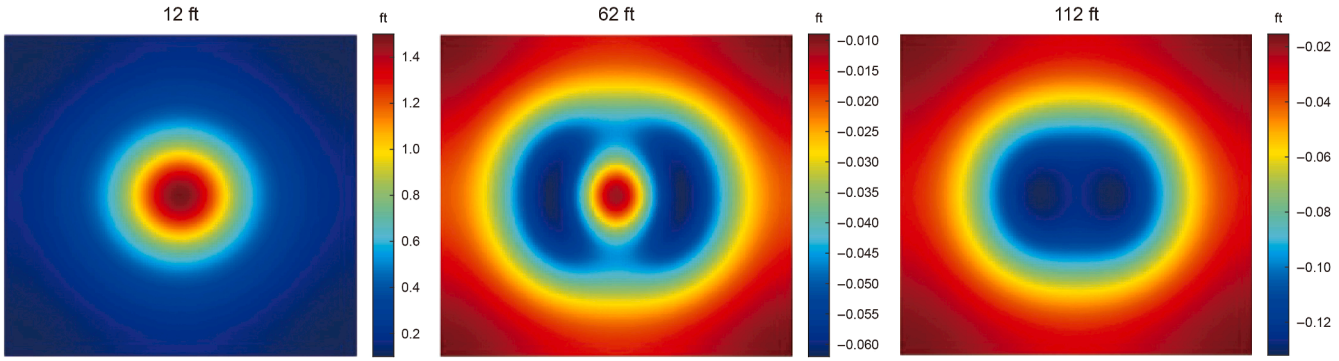

Fig. 14. Profiles of the surface movement with different length of the injection well. Left: injection well is 12 ft long. Middle: injection well is 62 ft long. Right: injection well is 112 ft long. The spatial dimension is the same as that in Fig. 13. Positive values of the surface movement mean upward movements.

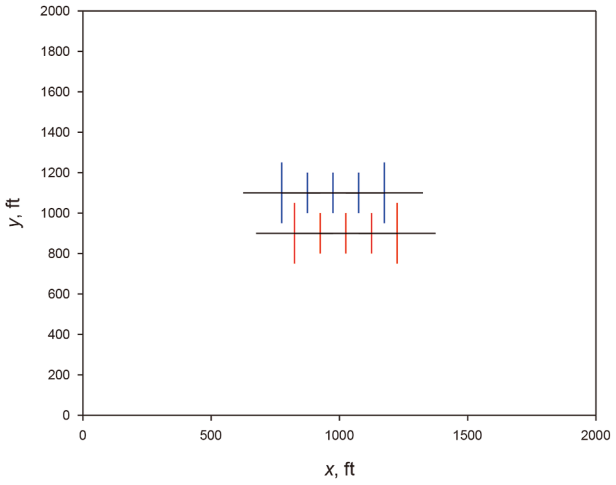

Fig. 15. Birdview of two horizontal wells with zipper-type fractures. The black lines indicate the horizontal wells, while the blue/red lines indicate fractures.

Zhou's model for the fluid flow is limited to infinite domain assumption without mechanical effect. Hence, the current assumption of infinite fracture permeability can be relaxed. Our model can not only calculate the pressure but also the stress, therefore it can predict the effective closure stress on the fracture plane. Hence, the compaction effect of the fracture can be potentially taken into consideration.

Admittedly, this solution still has certain limitations. First of all, it is not close-formed in the original domain, causing some inconvenience in the implementation. Secondly, it can only handle sources with given production rates and cannot be applied to cases where bottom hole pressure is specified. Thirdly, the rock permeability is stress-independent, which could be a strong assumption in practice, particularly for tight and shale reservoirs. Fourthly, the model, like most analytical models, is only applicable to single-phase flows. The applicability of our model to multiphase flow problems, such as condensate gas reservoirs or volatile oil reservoirs, is limited due to the nonlinear nature of the problem. For fast prediction of the multiphase process, linearization of the governing equation may be needed (Deng and King, 2015; Liao, 2004). Moreover, machine learning methods are promising alternatives (Li et al., 2021; Bi et al., 2023). We therefore propose to continue the efforts in extending the current solution to broader scenarios.

Table 5
Input parameters of the stress inference case study.

Parameters	Values	Units
Rock porosity ϕ	0.05	Dimensionless
Poisson's ratio ν	0.2	Dimensionless
Biot's coefficient α	0.9	Dimensionless
Biot's modulus M	1.5×10^6	psi
Young's modulus E	4.0×10^6	psi
Liquid viscosity μ	1.0	cP
Liquid density ρ	65	lbm/ft^3
Fracture height	60	ft
Liquid production rate Q	750	bbl/d/well
Production duration t	200	d

CRediT authorship contribution statement

Shihao Wang: Writing – original draft, Methodology, Formal analysis, Conceptualization. **Ouassim Khebzegga:** Writing – review & editing, Validation.

Declaration of competing interest

The authors declare that they have no known competing financial interests or personal relationships that could have appeared to influence the work reported in this paper.

Appendix A. Formulation of integral transforms

In this appendix, we briefly introduce the integral transforms used in this work.

The Laplace transform is defined as

$$L\{f\}(s) = \int_0^\infty f(x)\mathrm{e}^{-sx}\mathrm{d}x \tag{A-1}$$

The Fourier transform is defined as

$$F_x\{f\}(q_x) = \int_{-\infty}^{\infty} f(x)\mathrm{e}^{-iq_x x}\mathrm{d}x \tag{A-2}$$

Particularly, the conversion of the sink/source term to the Fourier domain is then

$$F_x\left(F_y(\mathrm{Q})\right) = F_x\left(F_y(Q(t)\cdot\delta(D,0,H))\right) = Q(t)\mathrm{e}^{iq_x D}\delta(z-H) \tag{A-3}$$

We use the built-in functions in MATLAB to conduct the inverse integral transform calculations.

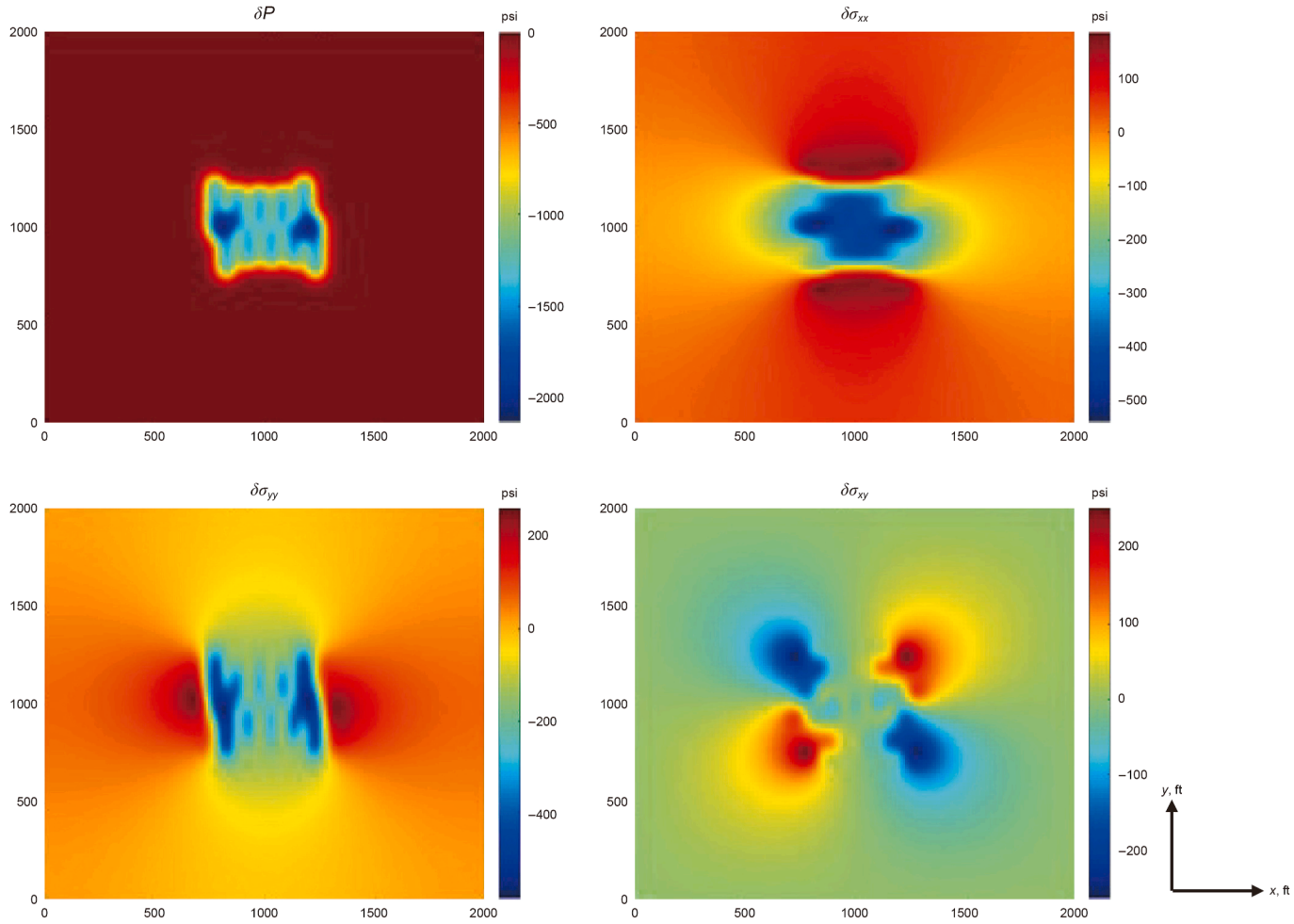

Fig. 16. The variation of pressure, normal and shear stress at the layer of production for the low-permeability case.

Appendix B. Transformed stress and displacement variables

This appendix lists the formulations of the transformed stress and displacement variables.

$$\frac{\mathrm{d}^2(\delta\bar{u}_x)}{\mathrm{d}z^2}-\left(q_x^2+q_y^2\right)\delta\bar{u}_x+iq_x\frac{3}{(2\nu+2)G}\delta\bar{\sigma}_{\mathrm{m}}-iq_x\alpha\frac{1-2\nu}{(2\nu+2)G}\delta\bar{P}=0 \tag{B-1}$$

$$\frac{\mathrm{d}^2(\delta\bar{u}_y)}{\mathrm{d}z^2}-\left(q_x^2+q_y^2\right)\delta\bar{u}_y+iq_y\frac{3}{(2\nu+2)G}\delta\bar{\sigma}_{\mathrm{m}}-iq_y\alpha\frac{1-2\nu}{(2\nu+2)G}\delta\bar{P}=0 \tag{B-2}$$

$$\frac{\mathrm{d}^2(\delta\bar{u}_z)}{\mathrm{d}z^2}-\left(q_x^2+q_y^2\right)\delta\bar{u}_z+\frac{3}{(2\nu+2)G}\frac{\mathrm{d}(\delta\bar{\sigma}_{\mathrm{m}})}{\mathrm{d}z}-\alpha\frac{1-2\nu}{(2\nu+2)G}\frac{\mathrm{d}(\delta\bar{P})}{\mathrm{d}z}=0 \tag{B-3}$$

$$\frac{\mathrm{d}^2(\delta\bar{\sigma}_{\mathrm{m}})}{\mathrm{d}z^2}=\alpha\frac{2(1-2\upsilon)}{3(1-\upsilon)}\frac{\mathrm{d}^2(\delta\bar{P})}{\mathrm{d}z^2} \tag{B-4}$$

where the superscript ¯ denotes that the variable below is in the Fourier–Laplace domain. Similarly, we can convert the mechanical constitutive relationship to the following relationships between the stress and displacements, as below.

$$\delta\bar{\sigma}_{xx}=iq_x\frac{E}{1+\nu}\delta\bar{u}_x+\frac{3\nu}{1+\nu}\delta\bar{\sigma}_{\mathrm{m}}+\alpha\frac{1-2\nu}{1+\nu}\delta\bar{P} \tag{B-5}$$

$$\delta\bar{\sigma}_{yy}=iq_y\frac{E}{1+\nu}\delta\bar{u}_y+\frac{3\nu}{1+\nu}\delta\bar{\sigma}_{\mathrm{m}}+\alpha\frac{1-2\nu}{1+\nu}\delta\bar{P} \tag{B-6}$$

$$\delta\bar{\sigma}_{zz}=\frac{E}{1+\nu}\frac{\mathrm{d}(\delta\bar{u}_z)}{\mathrm{d}z}+\frac{3\nu}{1+\nu}\delta\bar{\sigma}_{\mathrm{m}}+\alpha\frac{1-2\nu}{1+\nu}\delta\bar{P} \tag{B-7}$$

$$\delta\bar{\tau}_{xz}=\frac{E}{2(1+\nu)}\left(\frac{\mathrm{d}(\delta\bar{u}_x)}{\mathrm{d}z}+iq_x\delta\bar{u}_z\right) \tag{B-8}$$

$$\delta\bar{\tau}_{yz}=\frac{E}{2(1+\nu)}\left(\frac{\mathrm{d}(\delta\bar{u}_y)}{\mathrm{d}z}+iq_y\delta\bar{u}_z\right) \tag{B-9}$$

$$\delta\bar{\tau}_{xy}=\frac{E}{2(1+\nu)}\left(iq_x\delta\bar{u}_y+iq_y\delta\bar{u}_x\right) \tag{B-10}$$

Appendix C. Solution procedure of Eq. (19)

Eq. (19) is also a second order non-homogeneous ODE. To get its solution, we decompose its non-homogeneous term (right-side terms in Eq. (19) into three parts, resulting in three equations, as below.

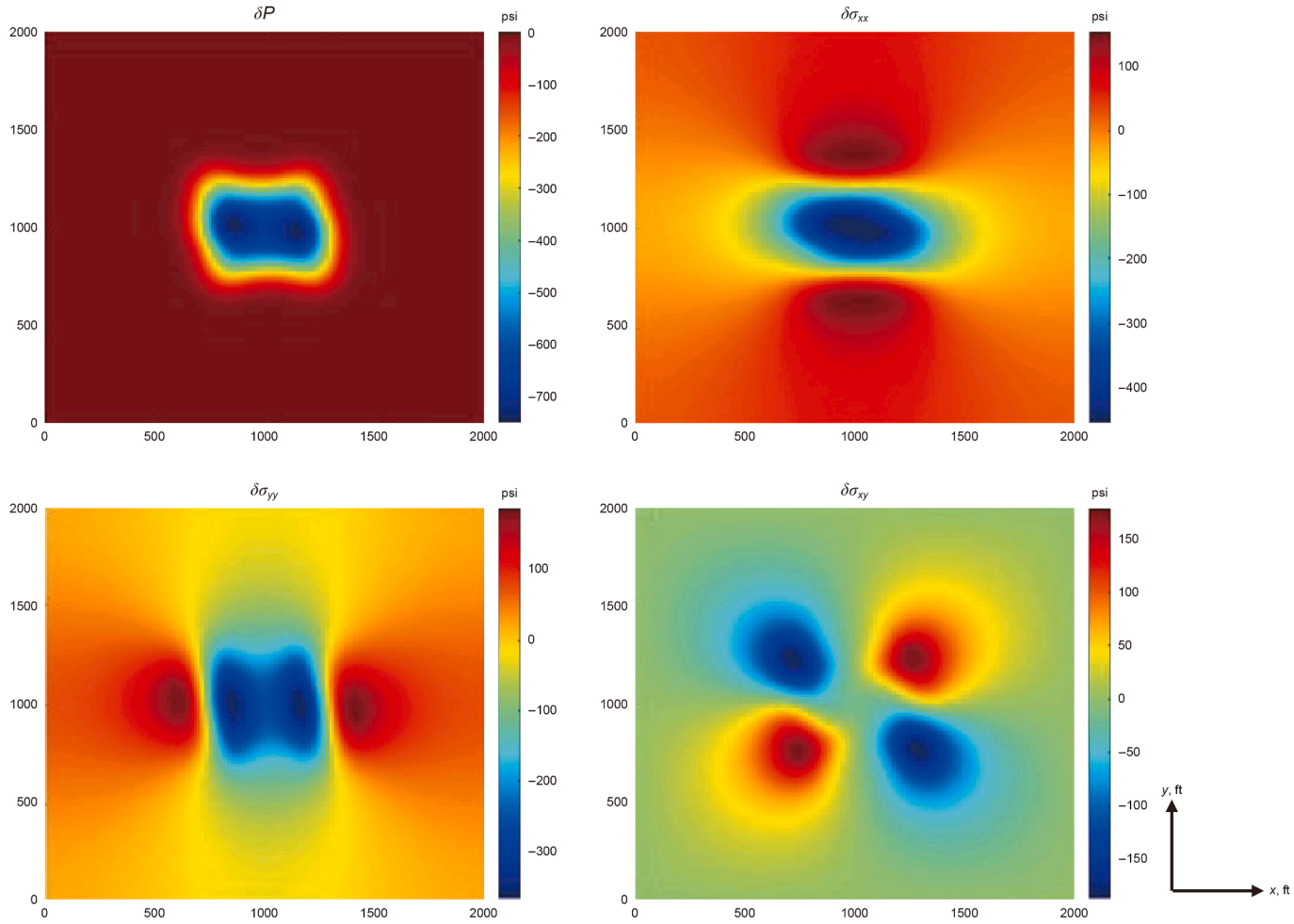

Fig. 17. The variation of pressure, normal and shear stress at the layer of production for the high-permeability case.

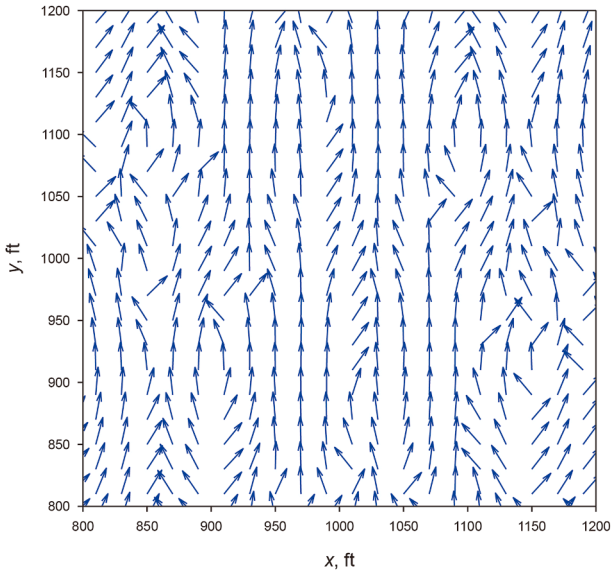

Fig. 18. The profile of the re-orientation of the maximum horizontal stress in the fracture tip region in the low-permeability case.

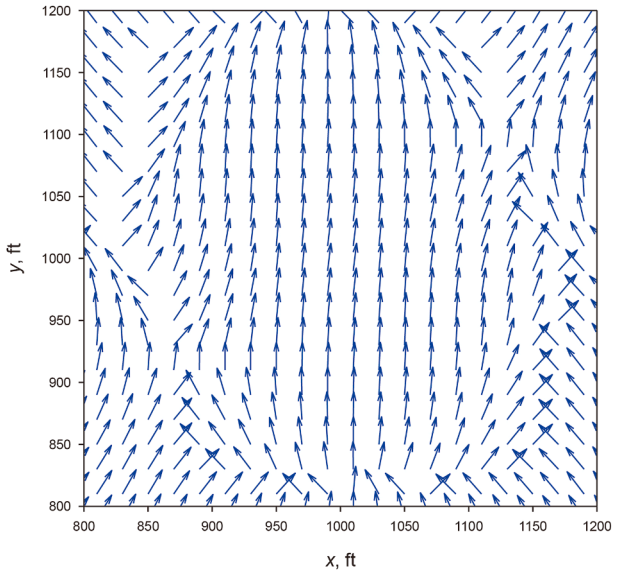

Fig. 19. The profile of the re-orientation of the maximum horizontal stress in the fracture tip region in the high-permeability case.

$$\begin{cases} \dfrac{d^2(\delta\overline{P}_1)}{dz^2}(z,s) - m^2\delta\overline{P}_1(z,s) = A_a a_1 e^{qz} \\ \dfrac{d^2(\delta\overline{P}_2)}{dz^2}(z,s) - m^2\delta\overline{P}_2(z,s) = A_a a_2 e^{-qz} \\ \dfrac{d^2(\delta\overline{P}_3)}{dz^2}(z,s) - m^2\delta\overline{P}_3(z,s) = \dfrac{\mu}{k}\overline{Q}(s)e^{iq_xD}\delta(z-H) \end{cases} \tag{C-1}$$

with

$$A_a = -\frac{\mu}{k}\frac{\alpha}{\lambda+\frac{2}{3}G}s$$

$$A_Q = \frac{\mu}{k}e^{iq_xD}$$

Each of the above equations corresponds to a particular solution of the original ODE, and the solution $\delta\overline{P}$ can be obtained by the superposition of the particular solutions and a general solution, as $\delta\overline{P} = \delta\overline{P}_0 + \delta\overline{P}_1 + \delta\overline{P}_2 + \delta\overline{P}_3$, where $\overline{P}_0$ is the general solution of the homogeneous version of the ODE.

Clearly, $\overline{P}_0$ is linear proportional to e^{-mz}, as below.

$$\delta\overline{P}_0 = a_p e^{-mz} \tag{C-2}$$

where a_p is the constant to be determined by the boundary condition.

Since the pressure change at infinity should fade to zero, a_1 must be zero. Therefore $\delta\overline{P}_1$ can be consolidated into the homogeneous solution $\delta\overline{P}_0$.

$\delta\overline{P}_2$ is solved as follows

$$\delta\overline{P}_2 = \frac{1}{q^2-m^2}A_a a_2 e^{-qz} \tag{C-3}$$

Since m is not equal to q, the above formulation avoids the degeneration case where m is equal to q.

$\delta\overline{P}_3$ can be solved using the method of variation of parameters (Arnol'd 1992), as

$$\delta\overline{P}_3 = -\frac{1}{2m}e^{-m|z-H|}A_Q\overline{Q} \tag{C-4}$$

Combining Eqs. (C-2) to (C-4) with the boundary conditions, the constant a_p is solved as

$$a_p = -\frac{1}{m(q+m)}A_a a_2 - \frac{1}{2m}A_Q\overline{Q}e^{-mH} \tag{C-5}$$

It should be noted that the above method can be easily extended to other boundary conditions at the top surface. For instance, if there is an influx term (time-dependent or time-independent) at the ground surface, one only needs to transform it to the Fourier–Laplace then combine it with Eqs. (C-2) to (C-4), leading to a different expression of a_p.

Appendix D. Formulation of the stress components in the Fourier–Laplace domain

In this appendix, we present the formulation of the stress in the Fourier–Laplace domain, and a flowchart of the solution process.

The six stress components are solved as below

$$\begin{aligned} \delta\overline{\sigma}_{xx} = {} & \frac{iq_x}{2q}\frac{E}{1+\nu}\left(a_2 iq_x\frac{3}{(2\nu+2)G} + \frac{1}{q^2-m^2}A_a a_2\right)ze^{-qz} + \left(-\frac{1}{2m}\frac{iq_x}{2q}\frac{E}{1+\nu}\frac{A_Q\overline{Q}}{q^2-m^2} - \alpha\frac{1-2\nu}{1-\nu}\frac{1}{2m}A_Q\overline{Q}\right)e^{-m|z-H|} \\ & + \left[\frac{iq_x}{2q}\frac{E}{1+\nu}\left(\frac{q}{m(q^2-m^2)}A_a a_2 + \frac{1}{2m}A_Q\overline{Q}e^{-mH}\right)\frac{1}{m^2-q^2} - \alpha\frac{1-2\nu}{1-\nu}\frac{1}{2m}A_Q\overline{Q}e^{-mH}\right]e^{-mz} + \left(\frac{3\nu}{1+\nu}a_2\right. \\ & \left. + \alpha\frac{1-2\nu}{1-\nu}\frac{1}{q^2-m^2}A_a a_2\right)e^{-qz} \end{aligned} \tag{D-1}$$

$$\begin{aligned} \delta\overline{\sigma}_{yy} = {} & \frac{iq_y}{2q}\frac{E}{1+\nu}\left(a_2 iq_y\frac{3}{(2\nu+2)G} + \frac{1}{q^2-m^2}A_a a_2\right)ze^{-qz} \\ & + \left(-\frac{1}{2m}\frac{iq_y}{2q}\frac{E}{1+\nu}\frac{A_Q\overline{Q}}{q^2-m^2} - \alpha\frac{1-2\nu}{1-\nu}\frac{1}{2m}A_Q\overline{Q}\right)e^{-m|z-H|} \\ & + \left[\frac{iq_y}{2q}\frac{E}{1+\nu}\left(\frac{q}{m(q^2-m^2)}A_a a_2 + \frac{1}{2m}A_Q\overline{Q}e^{-mH}\right)\frac{1}{m^2-q^2} - \alpha\frac{1-2\nu}{1-\nu}\frac{1}{2m}A_Q\overline{Q}e^{-mH}\right]e^{-mz} \\ & + \left(\frac{3\nu}{1+\nu}a_2 + \alpha\frac{1-2\nu}{1-\nu}\frac{1}{q^2-m^2}A_a a_2\right)e^{-qz} \end{aligned} \tag{D-2}$$

$$\begin{aligned}\delta\bar{\sigma}_{zz} &= \left(-\frac{B_q}{2q}\frac{E}{1+\nu}+\frac{3\nu}{1+\nu}a_2+\frac{1}{q^2-m^2}A_a a_2\right)e^{-qz}+\frac{E}{1+\nu}\frac{B_q}{2}ze^{-qz}\\ &-\left(\frac{E}{1+\nu}\frac{mB_m}{m^2-q^2}+\alpha\frac{1-2\nu}{1-\nu}\frac{q}{m(q^2-m^2)}A_a a_2\right.\\ &\left.+\alpha\frac{1-2\nu}{1-\nu}\frac{1}{2m}A_Q\bar{Q}e^{-mH}\right)e^{-mz}\\ &-\left(\frac{B_{|z-H|}}{q^2-m^2}\frac{m(H-z)}{|z-H|}\frac{E}{1+\nu}+\alpha\frac{1-2\nu}{1-\nu}\frac{1}{2m}A_Q\bar{Q}\right)e^{-m|z-H|}\end{aligned} \tag{D-3}$$

$$\begin{aligned}\delta\bar{\tau}_{xz} &= -\frac{1}{2}G\left(a_2 iq_x\frac{3}{(2\nu+2)G}+\frac{1}{q^2-m^2}A_a a_2+\frac{iq_x b_q}{2q}\right)ze^{-qz}\\ &+G\left(iq_x b_m-\frac{q}{(q^2-m^2)}A_a a_2-\frac{1}{2}A_Q\bar{Q}e^{-mH}\right)\frac{1}{m^2-q^2}e^{-mz}\\ &+\frac{1}{2q}G\left(a_2 iq_x\frac{3}{(2\nu+2)G}+\frac{1}{q^2-m^2}A_a a_2\right)e^{-qz}\\ &-G\left(\frac{1}{2}\frac{A_Q\bar{Q}}{q^2-m^2}\frac{(H-z)}{|z-H|}+\frac{iq_x b_{|z-H|}}{q^2-m^2}\right)e^{-m|z-H|}\end{aligned} \tag{D-4}$$

$$\begin{aligned}\delta\bar{\tau}_{yz} &= -\frac{1}{2}G\left(a_2 iq_y\frac{3}{(2\nu+2)G}+\frac{1}{q^2-m^2}A_a a_2+\frac{iq_y b_q}{2q}\right)ze^{-qz}\\ &+G\left(iq_y b_m-\frac{q}{(q^2-m^2)}A_a a_2-\frac{1}{2}A_Q\bar{Q}e^{-mH}\right)\frac{1}{m^2-q^2}e^{-mz}\\ &+\frac{1}{2q}G\left(a_2 iq_y\frac{3}{(2\nu+2)G}+\frac{1}{q^2-m^2}A_a a_2\right)e^{-qz}\\ &-G\left(\frac{1}{2}\frac{A_Q\bar{Q}}{q^2-m^2}\frac{(H-z)}{|z-H|}+\frac{iq_y b_{|z-H|}}{q^2-m^2}\right)e^{-m|z-H|}\end{aligned} \tag{D-5}$$

$$\begin{aligned}\delta\bar{\tau}_{xy} &= G\left\{\frac{1}{2q}\left(-q_x q_y a_2\frac{3}{(\nu+1)G}+\left(iq_x+iq_y\right)\frac{1}{q^2-m^2}A_a a_2\right)ze^{-qz}\right\}\\ &-\frac{1}{2m}\left(iq_x+iq_y\right)\frac{A_Q\bar{Q}}{q^2-m^2}e^{-m|z-H|}\\ &+\left(iq_x+iq_y\right)\left(\frac{q}{m(q^2-m^2)}A_a a_2+\frac{1}{2m}A_Q\bar{Q}e^{-mH}\right)\frac{1}{m^2-q^2}e^{-mz}\end{aligned} \tag{D-6}$$

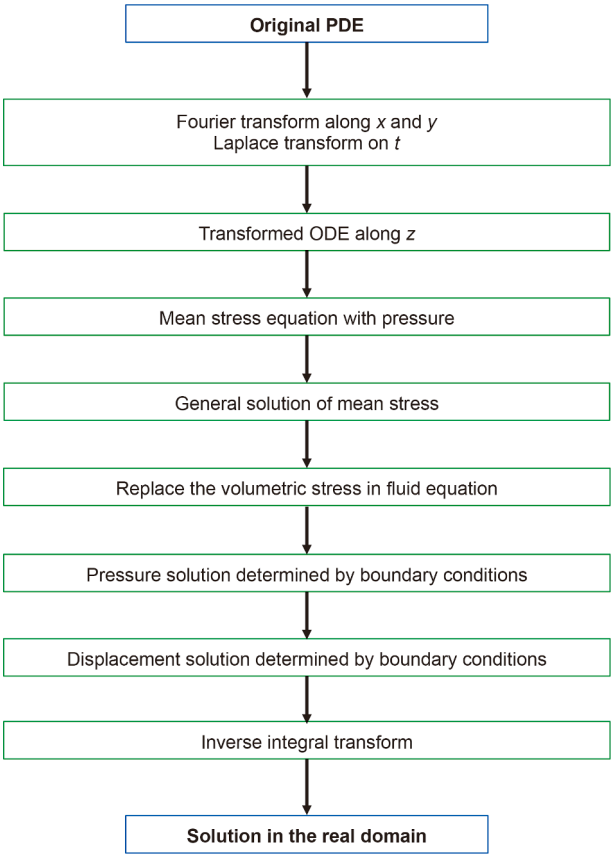

Fig. D-1. Flowchart of the solution procedure.

References

Abousleiman, Y., Cheng, A.H.-D., Cui, L., Detournay, E., Roegiers, J.-C., 1996. Mandel's problem revisited. Geotechnique 46 (2), 187–195. https://doi.org/10.1680/geot.1996.46.2.187.

Akbarpour, M., Abdideh, M., 2020. Wellbore stability analysis based on geomechanical modeling using finite element method. Model. Earth Syst. Environ. 6 (2), 617–626. https://doi.org/10.1007/s40808-020-00716-x.

Alshits, V.I., Kirchner, H.O.K., Maugin, G.A., 2001. Elasticity of multilayers: Properties of the propagator matrix and some applications. Math. Mech. Solid 6 (5), 481–502. https://doi.org/10.1177/108128650100600501.

Alvarez, J., Yared, K., Lewis, A., Aviles, I., Zhang, Z., Tang, J., et al., 2025. Numerical simulation of inter-well fracturing interference and fault reactivation in layered shale based on discrete lattice method. In: SPE/AAPG/SEG Unconventional Resources Technology Conference. https://doi.org/10.15530/urtec-2025-4265852.

Arnol'd, V.I., 1992. Ordinary Differential Equations. Springer-Verlag. http://repository.vnu.edu.vn/handle/VNU_123/80358.

Bi, J., Li, J., Wu, K., Chen, Z., Chen, S., Jiang, L., et al., 2023. A physics-informed spatial-temporal neural network for reservoir simulation and uncertainty quantification. SPE J. 29 (4), 2026–2043. https://doi.org/10.2118/212839-PA.

Biot, M.A., Romain, J.E., 1965. Mechanics of incremental deformations. Phys. Today 18, 68. https://doi.org/10.1063/1.3047001.

Bufler, H., 1971. Theory of elasticity of a multilayered medium. J. Elasticity 1 (2), 125–143. https://doi.org/10.1007/BF00046464.

Chen, L., Wang, Z., Peng, X., Yang, J., Wu, P., Lian, H., 2021. Modeling pressurized fracture propagation with the isogeometric BEM. Geomech. Geophys. Geo-energ. Geo-resour. 7 (3), 1–16. https://doi.org/10.1007/s40948-021-00248-3.

Cheng, A.H.-D., Badmus, T., Beskos, D.E., 1991. Integral equation for dynamic poroelasticity in frequency domain with bem solution. J. Eng. Mech. 117 (5), 1136–1157. https://doi.org/10.1061/(ASCE)0733-9399(1991)117:5(1136).

Crouch, S.L., 1976. Solution of plane elasticity problems by the displacement discontinuity method. I. Infinite body solution. Int. J. Numer. Methods Eng. 10 (2), 301–343. https://doi.org/10.1002/nme.1620100206.

Deng, L., King, M.J., 2015. Capillary corrections to buckley-leverett flow. In: SPE Annual Technology Conference and Exhibition. https://doi.org/10.2118/175150-MS.

Dong, C.Y., de Pater, C.J., 2001. Numerical implementation of displacement discontinuity method and its application in hydraulic fracturing. Comput. Methods Appl. Mech. Eng. 191 (8), 745–760. https://doi.org/10.1016/S0045-7825(01)00273-0.

Du, X., Cheng, L., Fang, M., Rao, X., Fang, S., Cao, R., 2024. An efficient coupled fluid flow-geomechanics model for capturing the dynamic behavior of fracture

systems in tight porous media. Eng. Anal. Bound. Elem. 169, 106046. https://doi.org/10.1016/j.enganabound.2023.10.046.
Geertsma, J., 1973. Land subsidence above compacting oil and gas reservoirs. J. Pet. Technol. 25 (6), 734–744. https://doi.org/10.2118/3734-PA.
Guo, X., Wu, K., An, C., Tang, J., Killough, J., 2019. Numerical investigation of effects of subsequent parent-well injection on interwell fracturing interference using reservoir-geomechanics-fracturing modeling. SPE J. 24 (4), 1884–1902. https://doi.org/10.2118/193853-PA.
Hanak, E., Escriva-Bou, A., Gray, B., Green, S., Harter, T., Jezdimirovic, J., et al., 2019. Water and the Future of the San Joaquin Valley: An Overview. Public Policy Institute of California. https://policycommons.net/artifacts/12244059/water-and-the-future-of-the-san-joaquin-valley/13137912/.
Hui, G., Chen, S., Gu, F., 2024. Strike–slip fault reactivation triggered by hydraulic-natural fracture propagation during fracturing stimulations near Clark Lake, Alberta. Energy Fuels 38 (19), 18547–18555. https://doi.org/10.1021/acs.energyfuels.4c02894.
Jaeger, J., Cook, N., Zimmerman, R., 2007. Fundamentals of Rock Mechanics, Fourth ed. Wiley https://www.wiley.com/en-us/Fundamentals+of+Rock+Mechanics%2C+4th+Edition-p-9780632057597.
Jeffreys, H., Swirles, B., Morse, P.M., 1956. Methods of mathematical physics. Phys. Today 9, 32. https://doi.org/10.1063/1.3060205.
Jin, B., Liu, H., 2001. Dynamic response of a poroelastic half space to horizontal buried loading. Int. J. Solid Struct. 38 (44), 8053–8064. https://doi.org/10.1016/S0020-7683(01)00115-4.
Khebzegga, O., Chen, Y., Rey, A., Wang, B., 2022. Integrating geomechanics studies to shale and tight phased development - application to Delaware Basin. In: SPE/AAPG/SEG Unconventional Resources Technology Conference. https://doi.org/10.2118/212224-MS.
Li, Z., Kovachki, N., Azizzadenesheli, K., Liu, B., Bhattacharya, K., Stuart, A., et al., 2021. Fourier neural operator for parametric partial differential equations. arXiv. http://arxiv.org/abs/2010.08895.
Liao, S., 2004. On the homotopy analysis method for nonlinear problems. Appl. Math. Comput. 147 (2), 499–513. https://doi.org/10.1016/S0096-3003(02)00790-7.
Liu, Y.-H., Zhang, J.-T., Bai, J., Zhang, F.-S., Tang, J.-Z., 2023. Numerical study of hydraulic fracturing in the sectorial well-factory considering well interference and stress shadowing. Pet. Sci. 20 (6), 3567–3581. https://doi.org/10.1016/j.petsci.2023.08.016.
Liu, Z., Liu, R., 2018. A fully implicit and consistent finite element framework for modeling reservoir compaction with large deformation and nonlinear flow model. Part I: Theory and formulation. Comput. Geosci. 22 (3), 623–637. https://doi.org/10.1007/s10596-018-9717-6.
Lu, J.-F., Hanyga, A., 2005. Fundamental solution for a layered porous half space subject to a vertical point force or a point fluid source. Comput. Mech. 35 (5), 376–391. https://doi.org/10.1007/s00466-004-0626-7.
Ma, S., Gutierrez, M., 2021. Determination of the poroelasticity of shale. Acta Geotech. 16 (2), 581–594. https://doi.org/10.1007/s11440-020-01048-2.
Ma, X., Zoback, M.D., 2017. Laboratory experiments simulating poroelastic stress changes associated with depletion and injection in low-porosity sedimentary rocks. J. Geophys. Res. Solid Earth 122 (4), 2478–2503. https://doi.org/10.1002/2016JB013668.
Manchanda, R., Bhardwaj, P., Hwang, J., Sharma, M.M., 2018. Parent-child fracture interference: Explanation and mitigation of child well underperformance. In: SPE Hydraulic Fracturing Technology Conference. https://doi.org/10.2118/189849-MS.
Pan, E., 1989. Static response of a transversely isotropic and layered half-space to general surface loads. Phys. Earth Planet. Inter. 54 (3), 353–363. https://doi.org/10.1016/0031-9201(89)90252-5.
Pan, L.-H., Hou, P.-F., Chen, J.-Y., 2016. 2D steady-state general solution and fundamental solution for fluid-saturated, orthotropic, poroelastic materials. Z. Angew. Math. Phys. 67 (4), 84. https://doi.org/10.1007/s00033-016-0676-z.
Peirce, A.P., Siebrits, E., 2001. The scaled flexibility matrix method for the efficient solution of boundary value problems in 2D and 3D layered elastic media. Comput. Methods Appl. Mech. Eng. 190 (45), 5935–5956. https://doi.org/10.1016/S0045-7825(01)00206-7.
Philippacopoulos, A.J., 1997. Buried point source in a poroelastic half-space. J. Eng. Mech. 123 (8), 860–869. https://doi.org/10.1061/(ASCE)0733-9399(1997)123:8(860).
Pruess, K., 1991. TOUGH2: a general-purpose numerical simulator for multiphase fluid and heat flow. NASA STI/Recon Tech. Rep. 92, 14316.
Rajapakse, R.K.N.D., Senjuntichai, T., 1993. Fundamental solutions for a poroelastic half-space with compressible constituents. J. Appl. Mech. 60 (4), 847–856. https://doi.org/10.1115/1.2900992.
Ravaji, B., Mashadizade, S., Hashemi, A., 2018. Introducing optimized validated meshing system for wellbore stability analysis using 3D finite element method. J. Nat. Gas Sci. Eng. 53, 74–82. https://doi.org/10.1016/j.jngse.2018.01.042.
Rutqvist, J., 2011. Status of the TOUGH-FLAC simulator and recent applications related to coupled fluid flow and crustal deformations. Comput. Geosci. 37 (6), 739–750. https://doi.org/10.1016/j.cageo.2010.08.006.
Sac-Morane, A., Veveakis, M., Rattez, H., 2024. A phase-field discrete element method to study chemo-mechanical coupling in granular materials. Comput. Methods Appl. Mech. Eng. 424, 116900. https://doi.org/10.1016/j.cma.2024.116900.
Scherz, P.E., Pradhan, P.E., Rainbolt, P.E., 2020. Mitigation for fracture driven interaction: A Midland Basin case study. In: SPE Hydraulic Fracturing Technology Conference. https://doi.org/10.2118/199686-MS.
Segall, P., 1992. Induced stresses due to fluid extraction from axisymmetric reservoirs. PAGEOPH 139 (3), 535–560. https://doi.org/10.1007/BF00879950.
Selvadurai, A.P.S., 2007. The analytical method in geomechanics. Appl. Mech. Rev. 60, 87. https://doi.org/10.1115/1.2730845.
Senjuntichai, T., Rajapakse, R.K.N.D., 1994. Dynamic Green's functions of homogeneous poroelastic half-plane. J. Eng. Mech. 120 (11), 2381–2404. https://doi.org/10.1061/(ASCE)0733-9399(1994)120:11(2381).
Taguchi, I., Kurashige, M., 2002. Fundamental solutions for a fluid-saturated, transversely isotropic, poroelastic solid. Int. J. Numer. Anal. Methods GeoMech. 26 (3), 299–321. https://doi.org/10.1002/nag.204.
Wang, B., Zhou, Y., Li, K.M., Guyaguler, B., 2024. Coupling a simulator and at least one other simulator. U.S. Patent 12,181,623.
Wang, S., 2015. Numerical Study of Thermal-hydraulic-mechanical Behavior of Fractured Geothermal Reservoirs. M.S. Thesis. Colorado School of Mines. https://www.proquest.com/openview/301b25a70acf6d508fa95003440ff314/1?pq-origsite=gscholar&cbl=18750.
Wang, S., Wu, Y.-S., 2022. Theoretical analysis and semi-analytical formulation for capturing the coupled thermal-hydraulic-mechanical process using the stress formulation. J. Pet. Sci. Eng. 208, 109752. https://doi.org/10.1016/j.petrol.2021.109752.
Wang, S., Zhang, J., Yang, Z., Yin, C., Wang, Y., Zhang, R., et al., 2017. Fully coupled thermal-hydraulic-mechanical reservoir simulation with non-isothermal multiphase compositional modeling. In: SPE Reservoir Simulation Conference. https://doi.org/10.2118/182595-MS.
Wang, S., Di, Y., Winterfeld, P.H., Li, J., Zhou, X., Wu, Y.-S., et al., 2021. Understanding the multiphysical processes in carbon dioxide enhanced-oil-recovery operations: A numerical study using a general simulation framework. SPE J. 26 (2), 918–939. https://doi.org/10.2118/200465-PA.
Wang, S., Zhang, Y., Khebzegga, O., Wang, B., Liu, Z., Wen, X.-H., 2022a. A semi-analytical solution of the induced stress change in a layered reservoir based on the stress formulation. In: SPE/AAPG/SEG Unconventional Resources Technology Conference. https://doi.org/10.15530/urtec-2022-3705427.
Wang, S., Zhang, Y., Liu, Z., Wen, X., 2022b. A semianalytical formulation for estimating induced surface subsidence of a poroelastic reservoir. SPE J. 27 (5), 3158–3177. https://doi.org/10.2118/209605-PA.
Wang, S., Li, S., Wu, Y.-S., 2023a. An analytical solution of pressure and displacement induced by recovery of poroelastic reservoirs and its applications. SPE J. 28 (3), 1329–1348. https://doi.org/10.2118/212850-PA.
Wang, S., Yu, X., Winterfeld, P.H., Wu, Y.-S., 2023b. Real-time simulation of hydraulic fracturing using a combined integrated finite difference and discontinuous displacement method: Numerical algorithm and field applications. Water 15 (5), 938. https://doi.org/10.3390/w15050938.
Wang, Z., Guo, X., Zheng, G., Yu, P., Wang, W., Jin, Y., et al., 2022c. Effects of parent well spacing on the poroelastic behaviors in the infill zone in shale oil reservoirs: A case study in Jimsar Shale Oil, China. Energy Sci. Eng. 10 (4), 1043–1054. https://doi.org/10.1002/ese3.1077.
Weng, M.-C., Peng, C.-H., Le, H.-K., Shiu, W.-J., Fang, C.-H., 2024. Discrete element analysis of hydraulic stimulation in a slate geothermal reservoir using the ubiquitous foliation model. Geomech. Geophys. Geo-energ. Geo-resour. 10 (1), 1–23. https://doi.org/10.1007/s40948-023-00688-2.
Wu, K., Olson, J.E., 2016. Mechanisms of simultaneous hydraulic-fracture propagation from multiple perforation clusters in horizontal wells. SPE J. 21 (3), 1000–1008. https://doi.org/10.2118/179122-PA.
Wu, R., Liu, X., Singh, A., Wang, B., Li, Y., 2022. Investigation of subsurface mechanism impacting parent well pressure response during fracture driven interactions using coupled geomechanics, fluid flow, fracture propagation modeling. In: SPE/AAPG/SEG Unconventional Resources Technology Conference. https://doi.org/10.15530/urtec-2022-3726016.
Xiao, S., Yue, Z.Q., Xiao, H., 2019. Boundary element analysis of transversely isotropic bimaterial halfspaces with inclined planes of isotropy and interfaces. Int. J. Numer. Anal. Methods GeoMech. 43 (17), 2599–2627. https://doi.org/10.1002/nag.2995.
Yu, X., Winterfeld, P., Wang, S., Wang, C., Wang, L., Wu, Y., 2019. A geomechanics-coupled embedded discrete fracture model and its application in geothermal reservoir simulation. In: SPE Reservoir Simulation Conference. https://doi.org/10.2118/219578-MS.
Yu, X., Yan, X., Wang, C., Wang, S., Wu, Y.-S., 2023. Thermal-hydraulic-mechanical analysis of enhanced geothermal reservoirs with hybrid fracture patterns using a combined XFEM and EDFM-MINC model. Geoenergy Sci. Eng. 228, 211984. https://doi.org/10.1016/j.geoen.2023.211984.
Zhang, Z., Tang, J., Zhang, J., Meng, S., Li, J., 2024. Modeling of scale-dependent perforation geometrical fracture growth in naturally layered media. Eng. Geol. 336, 107499. https://doi.org/10.1016/j.enggeo.2024.107499.
Zhou, W., Banerjee, R., Poe, B., Spath, J., Thambynayagam, M., 2013. Semianalytical production simulation of complex hydraulic-fracture networks. SPE J. 19 (1), 6–18. https://doi.org/10.2118/152067-PA.